



Synthesis of nanomagnetite/copper oxide/potassium carrageenan nanocomposite for the adsorption and Photo-Fenton degradation of Safranin-O: kinetic and thermodynamic studies

Asaad. F. Hassan¹ · Laila M. Alshandoudi² · Aya M. Awad¹ · Ahmed A. Mustafa¹ · Ghada Esmail¹

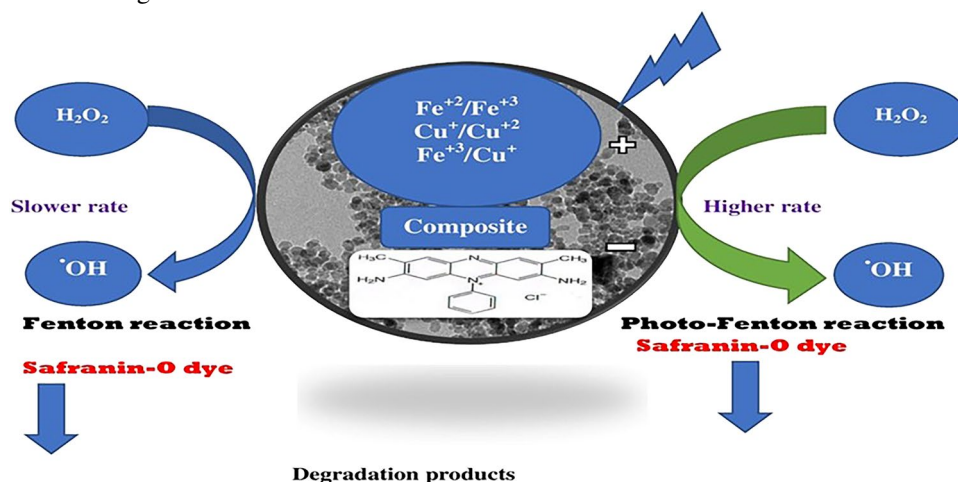
Received: 19 December 2022 / Revised: 21 February 2023 / Accepted: 26 February 2023 / Published online: 27 March 2023
© The Author(s) 2023

Abstract

In the current study, a novel nanomaterial called nanomagnetite/copper oxide/potassium carrageenan nanocomposite (MKCO) was fabricated to include Fenton (nanomagnetite, NM) and Fenton-like reagent (copper oxide nanoparticles, NCO) in a matrix of potassium carrageenan biopolymer. The prepared solid materials were characterized by different physicochemical techniques, such as TGA, N₂ adsorption/desorption, SEM, TEM, XRD, DRS, pH_{PZC}, and FTIR. The prepared MKCO showed unique properties like higher specific surface area of 652.50 m²/g, pore radius of 1.19 nm, pH_{PZC} equals 7.80, and the presence of different surface chemical functional groups. Under various application conditions, comparative experiments between Safranin-O dye (SO) adsorption and Photo-Fenton catalytic degradation were conducted. After 24 h, MKCO had a maximum adsorption capacity of 384.61 mg/g at 42 °C, while the Photo-Fenton oxidation process took only 10 min to totally decompose 93% of SO at 21 °C. Based on the higher values of correlation coefficients, Langmuir's adsorption model is the best-fitted adsorption model for SO onto all the prepared solid materials. Studies on SO adsorption's kinetics and thermodynamics show that it is physisorption and that it operates according to endothermic, spontaneous, and PFO model processes. While, PFO, endothermic, and non-spontaneous processes are satisfied by the catalytic decomposition of SO. After five application cycles, MKCO demonstrated good catalyst reusability with a 3.4% decrease in degrading efficiency. For lower contaminant concentrations and shorter application times, Photo-Fenton catalytic degradation of organic pollutants is more effective than adsorption.

Graphical abstract

Fenton and Photo-Fenton degradation of Safranin-O

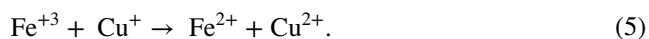
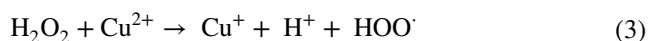
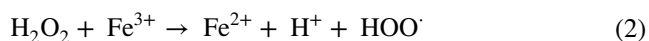


Keywords Nanomagnetite · Composite · Nanoparticles · *K*-carrageenan · Safranin-O · Adsorption · Degradation

Extended author information available on the last page of the article

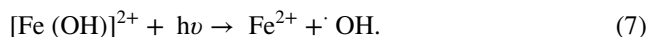
1 Introduction

Synthetic dyes are the most prevalent organic pollutants, and their toxicity to water resources is one of the most urgent problems facing modern society [1]. Numerous industries, including those in the textile, printing, paper, cosmetics, and leather dyeing industries, employ synthetic dyes on a large scale. These dyes have a number of drawbacks, including aesthetic and eutrophication pollution, as well as mutagenic and carcinogenic disorders [2]. Basic dyes like the cationic Safranin-O are frequently used in biological laboratories and the textile industry [3]. Safranin-O causes irreparable damage to the conjunctiva and cornea by stimulating the respiratory tract and the skin. For the treatment of organic dye wastewater, a variety of treatments, including biological treatment, adsorption, coagulation, and chemical oxidation approaches, have been used. Adsorption techniques are frequently used to remove dyes from aqueous media, because they have a greater removal effectiveness, are inexpensive, have simple operating steps, and can reuse solid adsorbents. Also, advanced oxidation processes (AOPS) are considered a potential, cost-effective, and efficient way for the complete degradation of non-biodegradable lower concentrations of organic contaminants in textile wastewater [4, 5]. Due to its low cost and simple implementation procedure, Fenton reaction is the greatest form of AOPS with superior technology [6]. Generally, hydroxyl radical ($\cdot\text{OH}$) produced from the combination between Fenton's ($\text{Fe}^{+2}/\text{H}_2\text{O}_2$) and Fenton-like reagent ($\text{Cu}^+/\text{H}_2\text{O}_2$) is the most reactive species with a high potential (2.8 eV), which is responsible for complete decomposition of non-degradable organic contaminants into safe H_2O , CO_2 , and inorganic ions. The rate of $\cdot\text{OH}$ production is increased by the formation of new Fe^{+2} due to the interaction between Fe^{+3} ions and Cu^+ (Eq. 5). The coexistence of iron and copper in the same solid composite will speed up the redox system's process and increase the creation of radical species necessary for the breakdown of organic contaminants, according to the following equations [6, 7]:



Heterogeneous catalysis and homogenous catalysis are two classes of Fenton applications, but homogenous catalysis has only been applied in a limited number of situations

because of the low efficiency of H_2O_2 , harsh acidic environments, limited applied pH medium ($\text{pH} < 3$), decreasing iron activity, and rising sludge generation [8, 9]. Conversely, the Photo-Fenton process uses ultraviolet radiation (UV) as external energy to accelerate the degradation by converting Fe^{2+} to Fe^{3+} ions, increasing hydrogen peroxide decomposition into $\cdot\text{OH}$, and electron-hole pair ($e^- - h^+$) formation [10], which raise the rate of pollutant degradation using alternative faster reaction as presented by Eqs. 6, 7



Simple nanomagnetite (Fe_3O_4) has a number of drawbacks when used in the Fenton oxidation process such as the tendency to produce more stable species, precipitation of $[\text{Fe}(\text{H}_2\text{O})_6]^{3+}$ complex at $\text{pH} > 3$, and its high surface energy [11]. By adding polymeric materials [12], metal oxide [13], metal ions [14], and composite creation [15], numerous authors were able to increase the stability of nanomagnetite throughout the heterogeneous Fenton process.

Copper oxide nanoparticles exhibit special physicochemical characteristics. It is a low-cost, p-type semiconductor material with a band gap of 1.2 eV at ambient temperature that is non-toxic, highly chemically stable, and environment-friendly [6, 16]. In contrast to iron, copper is more suited for usage in the Fenton-like procedure, which may be applied with ease in a wide pH range. $\text{Fe}_3\text{O}_4/\text{CuO}$ as a hybrid oxide nanoparticles system may be utilized as an alternative catalyst with better catalytic properties in the Photo-Fenton reaction [17]. A natural anionic-sulfated polysaccharide called carrageenan can be found in many different red seaweeds. Composites made of hydrogels based on polysaccharides have clean surfaces, flexible polymer communities, chemical and physical stability, reusability, and multifunctionality. As a result, they effectively adsorb and remove a variety of contaminants, and their application in the removal of heavy metal ions and organic contaminants is growing quickly. Different types of polysaccharides-based hydrogel, such as magnetic sodium alginate/carboxymethyl cellulose [18], chitosan/orange peel hydrogel [19], calcium alginate/carboxymethylated chitosan/Na-bentonite [20], and graphene oxide-modified κ -carrageenan/sodium alginate double-network hydrogel [21], were used for the removal of Pb^{+2} , Cr^{+6} , Ni^{+2} , and antibiotic, respectively. Different types of carrageenan (*Kappa*, *Iota*, *Lambda*) are widely utilized in the pharmaceuticals, food sector, and bioengineering, containing one, two, and three sulfate groups in each disaccharide repeat unit, respectively. Nanomagnetite readily agglomerates in polar environments, such as water, changing their nature as nanoparticles. Coating nanomagnetite with polymer is one method to stop agglomeration and add a functional group

with a particular characteristic to the surface. Because of the anionic nature of *K*-carrageenan and the abundance of availability of functionalities, its hydrogels were also utilized as adsorbents to remove cationic dyes from wastewater.

In this study, nanomagnetite (NM), copper oxide nanoparticles (NCO), nanomagnetite/copper oxide (NMCO), and nanomagnetite/copper oxide/potassium carrageenan nanocomposite (MKCO) were prepared. Several methods were used to investigate the produced solid nanoparticles, including TGA, N₂ adsorption/desorption isotherms, SEM, TEM, EDX, XRD, DRS, and FTIR. Different application conditions, such as the impact of pH, dose, initial dye concentration, time, and temperature, were taken into consideration while studying Safranin-O adsorption and Photo-Fenton degradation. Kinetic, thermodynamic parameters, and catalyst reusability was discussed after five catalytic cycles.

2 Materials and methods

2.1 Materials

Iron (II) chloride tetrahydrate (FeCl₂·4H₂O, > 99%), Iron (III) chloride hexahydrate, (FeCl₃·6H₂O, 97%), and ethanol (99%) were obtained from Oxford Lab Fine Chem LLP, India. Safranin-O dye (C₂₀H₁₉ClN₄, > 85%) and *kappa*-carrageenan extracted from *Eucheuma cottonii* (red seaweed) were obtained from Sigma Aldrich Co., USA. Off white powder *kappa*-carrageenan is characterized by the molecular mass of 401.32 g/mol, molecular formula of C₁₂H₁₇O₁₃S, > 12% loss on drying, 5 mg/mL solubility in hot distilled water, and viscosity of 5–25 mPa s for 0.3% in water at 25 °C. Sodium hydroxide (≥ 98%), HCl (37%), H₂O₂ (50%), CuSO₄·5H₂O (> 98%), and concentrated NH₄OH (28%) were obtained from El-Nasr for chemical and pharmaceutical industrial Co., Egypt.

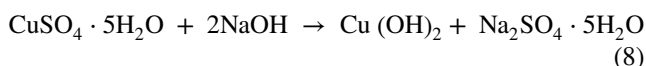
2.2 Preparation of solid materials

2.2.1 Preparation of nanomagnetite (NM)

Nanomagnetite was synthesized by co-precipitation method via mixing 2.21 g of iron (II) chloride tetrahydrate and 5.82 g of iron (III) chloride hexahydrate (1:2 molar ratio) with 175 mL deionized water in a three-neck flask in nitrogen gas medium. The previous mixture was heated at 80 °C by using a magnetic stirrer, and then, 15 mL of concentrated ammonium hydroxide was mixed as one dose. The resulting solution (black-colored) was heated for 10 min at 80 °C, filtered, washed by deionized water, and finally dried at 80 °C in an oven [9].

2.2.2 Preparation of copper oxide nanoparticles (NCO)

The sol–gel method was used to synthesized copper oxide nanoparticles. 0.1 M of CuSO₄·5H₂O was prepared in 100 mL of deionized water, and then, the mixture was continuously stirred until it became a totally uniform blue solution. Sodium hydroxide (0.2 M) was slowly added to the previous solution with stirring ultrasonically at 80 °C for about 2 h. The produced solution was cooled at room temperature, filtered, washed by ethanol, and dried in an oven at 60 °C. Then, the produced powder was incinerated at 400 °C for about 4 h. The following equations represent the synthesis procedures [22, 23]:



2.2.3 Preparation of nanomagnetite/copper oxide nanoparticles (NMCO)

Under ultrasonic settings, 100 mL of 0.1 M CuSO₄·5H₂O were mixed with 1.0 g of the produced nanomagnetite solid particles for 30 min. Sodium hydroxide solution (0.2 M) was added drop by drop to the previous solution with continuous ultrasonic stirring at 80 °C for 2 h. The produced, black-colored solution was cooled at room temperature, filtered, washed by ethanol, and dried at 60 °C, and then, the obtained black powder was incinerated at 400 °C for about 4 h.

2.2.4 Preparation of nanomagnetite/copper oxide/potassium carrageenan nanocomposite (MKCO)

First, nanomagnetite potassium carrageenan composite (NC) was prepared by dissolving 1.0 g of *kappa*-carrageenan into 50 mL of distilled water and mixed with 1.0 g of well-grinded nanomagnetite solid particles (NM) under continuous stirring at 80 °C. 10 g of KCl was mixed with 100 mL of distilled water in another beaker. Drop by drop, while stirring continuously, the *kappa*-carrageenan/nanomagnetite mixture was added to the KCl solution, and the finished solution was allowed to stand for 45 min. The final mixture was filtered, then washed with deionized water, and dried in an oven at 90 °C.

MKCO was prepared by mixing 1.0 g of NC composite solid particles into 100 mL of 0.1 M CuSO₄·5H₂O solution and kept under ultrasonic conditions for 30 min. Solution of sodium hydroxide (0.2 M) was slowly added to the previous solution and the final mixture was kept under ultrasonic

stirring for 1.0 h at 80 °C. The produced black solution was cooled at room temperature, filtered, washed with ethanol, and incinerated at 200 °C for 3 h.

2.3 Solid samples' characterization

The textural, thermal, and chemical properties of all the prepared solid nanoparticles were characterized using a variety of physicochemical techniques. Thermogravimetric analysis for NM, NCO, NMCO, and MKCO was tested by SDT Q600 V20.9 Build 20 instrument, UK under nitrogen flow rate (10 mL/min) with 5 °C/min as a heating rate up to 800 °C.

Textural characterizations, such as pore radius (\bar{r} , nm), total pore volume (V_T , cm³/g), and specific surface area (S_{BET} , m²/g) for NM, NCO, NMCO, and MKCO, were investigated by nitrogen gas adsorption using NOVA3200e gas sorption analyzer (Quantachrome Corporation, USA). The measured samples were degassed at 10⁻⁵ Torr and 150 °C for 15 h.

The morphological structure of NCO, NM, and MKCO as selected samples was investigated by scanning electron microscope (SEM) using the JEOL-JSM-7500 F instrument. Solid samples' surfaces were covered with 3.5 nm as a thin layer of gold using the vacuum evaporation technique.

Transmission electron microscope (TEM) for NM, NCO, and MKCO were studied through a JEOL-JEM-127 2100 (Tokyo, Japan) to determine the size, and shape of the samples. The investigated solid samples were dried at 120 °C and dispersed in ethanol under ultrasonic conditions for 10 min. A drop of the previous solution was placed onto a copper grid and coated with lacey carbon film.

Using the D8 Advance diffractometer, X-ray diffraction patterns (XRD) for NM, NCO, and MKCO were examined. XRD studies were investigated by using tiny powder from the solid sample and were exposed to Cu K α X-ray source ($\lambda = 1.5406 \text{ \AA}$) after placing onto the quartz plate. The radiation source operates at a current of 40 mA and 40 kV volt with Ni-filtered radiation.

Diffuse reflectance spectrophotometer (DRS) was carried out to calculate the range of light absorption and different energy band gaps (E_{bg} , eV) of NM, NCO, NMCO, and MKCO by a UV-Vis scanning spectrophotometer model, JASCO, Japan.

The point of zero charges (pH_{PZC}) of all synthesized materials (NM, NCO, NMCO, and MKCO) were studied by adding 30 mL of 0.1 M NaCl solutions in several Erlenmeyer flasks. pH values within each flask were adjusted between 1 and 12 using HCl and/or NaOH (0.05 M). Then, 0.025 g of prepared solid samples were added to each flask, the flasks were agitated for about 48 h, and pH_{final} values were measured by a pH meter, where pH_{PZC} is the point at which $\text{pH}_{\text{final}} = \text{pH}_{\text{initial}}$ [24].

The surface functional groups of NM, NCO, NMCO, and MKCO were determined using Fourier transform infrared (FTIR) spectroscopy utilizing a Mattson 5000 FTIR spectrometer from 400 to 4000 cm⁻¹. Solid discs were prepared in an agate mortar where 5 mg of the solid dried sample was mixed with 500 mg of KBr (ratio 1:100), and the previous mixture was pressed at 5 and 10 ton/cm³ for 5 and 7 min, respectively.

2.4 Adsorption of Safranin-O dye

To identify the ideal adsorption settings, maximal adsorption capacities, kinetic, and thermodynamic factors, batch adsorption studies of SO onto NM, NCO, NMCO, and MKCO were performed under various conditions. Adsorption of Safranin-O from aqueous solution onto NM, NCO, NMCO, and MKCO was studied under different applications condition, such as the effect of adsorbent dosage, pH, shaking time, initial dye concentration, and effect of temperature. After each experiment, Whatman filter paper grade 40 and Büchner funnel were used to filter the solution. The concentration of Safranin-O on filtrate was measured at (λ_{max} , 532 nm) using a UV-vis spectrophotometer. The removal (%) was calculated as indicated in the following equation:

$$\text{Removal (\%)} = \frac{(C_o - C_e)}{C_o} \times 100, \quad (10)$$

where C_o and C_e (mg/L) are SO concentrations at the beginning and equilibrium, respectively.

The effect of adsorbent dosage (0.06–2.0 g/L), pH (1–12), shaking time up to 48 h, initial dye concentration (5–650 mg/L), and the effect of temperature (25, 32, and 42 °C) were considered. The equilibrium adsorption capacity (q_e , mg/g) was calculated using the following equation:

$$q_e = \frac{(C_o - C_e)}{W} \times V. \quad (11)$$

The volume of the solution and the mass of the solid adsorbents are represented here as V (L) and W (g), respectively.

2.4.1 Models for adsorption isotherms

Adsorption isotherm models as Langmuir (Eq. 12), Freundlich (Eq. 14), Temkin (Eq. 15), and Dubinin-Radushkevich (Eq. 17) were applied to fit the data of SO adsorption onto all the prepared adsorbents [25, 26]

$$\frac{C_e}{q_e} = \frac{1}{bq_m} + \frac{C_e}{q_m} \quad (12)$$

$$R_L = \frac{1}{1 + bC_i} \tag{13}$$

Herein, q_m (mg/g), q_e (mg/g), b (L/mg), C_i (mg/L), and R_L are the maximum adsorption capacity, equilibrium adsorption capacity, Langmuir constant, initial concentration of dye, and dimensionless separation factor, respectively. R_L represents the nature of SO adsorption to be favorable if $0 < R_L < 1$, unfavorable in case of $R_L > 1$, linear in case of $R_L = 1$, and irreversible if R_L equals zero

$$\ln q_e = \ln K_F + \frac{1}{n} \ln C_e \tag{14}$$

where n and K_F (L/mg) are Freundlich constants related to the intensity of adsorption and the adsorption capacity, respectively

$$q_e = B \ln K_T + B \ln C_e \tag{15}$$

$$B = \frac{RT}{b_T} \tag{16}$$

Herein, b_T (J/mol), K_T (L/g), B (J/mol), and T (K), are Temkin constant, Temkin isotherm constant, the heat of adsorption constant, and absolute temperature, respectively. R is the ideal gas constant (8.314 J mol⁻¹ K⁻¹).

$$\ln q_e = \ln q_{DR} - K_{DR} \varepsilon^2 \tag{17}$$

$$\varepsilon = RT \ln \left(1 + \frac{1}{C_e} \right) \tag{18}$$

$$E_{DR} = \frac{1}{\sqrt{2K_{DR}}} \tag{19}$$

where E_{DR} , (kJ/mol), q_{DR} (mg/g), K_{DR} (mol²/kJ²), and ε are the mean adsorption energy, maximum adsorption capacity, activity coefficient, and Polanyi adsorption potential.

2.4.2 Kinetic adsorption models

To examine the kinetic parameters for SO adsorption onto the adsorbents, various kinetic models, including pseudo-first-order (PFO), pseudo-second-order (PSO), and Elovich equations [Eqs. (20–22)], were used [27, 28]

$$\ln(q_e - q_t) = \ln q_e - k_1 t \tag{20}$$

$$\frac{t}{q_t} = \frac{1}{k_2 q_e^2} + \frac{1}{q_e} t \tag{21}$$

$$q_t = \frac{\ln \alpha \beta}{\beta} + \frac{1}{\beta} \ln t \tag{22}$$

Herein, k_1 (h⁻¹), k_2 (g/mg h⁻¹), q_t (mg/g), α (mg/g h⁻¹), and β (g/mg) are PFO, PSO rate constants, adsorption capacity at time (t , hours), the starting rate of SO adsorption, and the activation energy of adsorption, respectively. The capacity of adsorption at a certain time (q_t , mg/g) is calculated using Eq. 23

$$q_t = \frac{(C_o - C_t)}{W} \times V, \tag{23}$$

where the equilibrium concentration of SO at a certain time (t) is denoted by C_t (mg/L).

2.4.3 Thermodynamic studies for SO adsorption

Thermodynamic parameters including equilibrium constant (K_d), the change of entropy (ΔS° , kJ mol⁻¹ K⁻¹), Gibbs free energy (ΔG° , kJ mol⁻¹), and enthalpy (ΔH° , kJ mol⁻¹) were studied for the evaluation of spontaneity, adsorption heat, and the ability of SO adsorption onto the surface of adsorbents. ΔS° and ΔH° were calculated from the intercept and slope of Vant’s Hoff equation (Eq. 25) [29]

$$K_d = \frac{C_s}{C_e} \tag{24}$$

$$\ln K_d = \frac{\Delta S^\circ}{R} - \frac{\Delta H^\circ}{RT} \tag{25}$$

$$\Delta G^\circ = \Delta H^\circ - T \Delta S^\circ \tag{26}$$

Here, K_d , C_s (mg/g), and C_e (mg/L) are the coefficient of distribution, the mass of surface adsorbed dye, and the equilibrium concentration of SO adsorption, respectively.

2.5 Degradation of Safranin-O by Fenton and Photo-Fenton process

Under various application conditions, heterogeneous Fenton oxidation of SO dye was studied using 100 mL of SO (5–40 mg/L), hydrogen peroxide (30–100 mmol), pH (2.2–6.0), catalyst dosage (0.8–2.0 g/L), and at a time up to 120 min in the presence of NM, NCO, NMCO, and MKCO. After equal time intervals, 2 mL of the solution was withdrawn and centrifuged after that the residual SO was determined using a UV–Vis spectrophotometer at SO λ_{max} (532 nm). Photo-Fenton degradation of SO dye was carried out using 100 mL of SO solution (10 mg/L), 50 mmol of H₂O₂, and 0.1 g of solid catalyst in the quartz glass box under continuous stirring. The previous solution mixture was illuminated by UV radiation using Philips TUV TL

11W Lamp, USA (254 nm) at a distance of 10 cm from the solution surface and the degradation rate was followed as in the previous experiment.

Various kinetic and thermodynamic models were examined with all of the generated solid catalysts (NM, NCO, NMCO, and MKCO). Kinetic studies were carried out using pseudo-first-order (Eq. 27). Thermodynamic studies were investigated to calculate thermodynamic parameters as activation energy (E_a , kJ/mol) using the Arrhenius model (Eq. 28), Gibbs free energy (ΔG^* , kJ/mol), change in enthalpy (ΔH^* , kJ/mol), and entropy (ΔS^* , kJ mol⁻¹ K⁻¹) were determined from Eqs. 29, 30 [30, 31]

$$\ln\left(\frac{C_o}{C_t}\right) = k_{app}t. \quad (27)$$

Herein, t (min), k_{app} (min⁻¹), C_t (mg/L), and C_o are irradiation time, the apparent first-order rate constant, and the residual concentrations after a certain time and initial concentrations of SO

$$\ln k = \ln A - \frac{E_a}{RT} \quad (28)$$

$$\ln\left(\frac{k}{T}\right) = -\frac{\Delta H^*}{RT} + \ln\left(\frac{K_b}{h}\right) + \frac{\Delta S^*}{R} \quad (29)$$

$$\Delta G^* = \Delta H^* - T\Delta S^*, \quad (30)$$

where A , k (min⁻¹), and E_a (kJ/mol) are the frequency factor constant, rate constant, and activation energy, respectively. R , T (K), h (6.623×10^{-34} J s), and K_b (1.3×10^{-23} J/K) are ideal gas constant, absolute temperature, Planck's and Boltzmann constants, respectively.

After five cycles of Photo-Fenton degradation of Safranin-O, the reusability of nanomagnetite/copper oxide/potassium carrageenan composite beads was examined. After each cycle, the solid catalyst was filtered, cleaned with deionized water, and dried at 80 °C for 3 h before being used in the following reuse cycle.

3 Results and discussion

3.1 Characterization of the prepared solid materials

Thermal analysis was done to examine the solid samples' thermal stability and the ratio of inorganic and organic components from room temperature to 800 °C, as shown in Fig. 1a. Thermal analysis of solid NM occurs in one stage and represents a tiny weight loss of < 4% at 800 °C which is related to surface and internal adsorbed water molecules and indicating its high thermal stability [9]. Degradation of

NCO and NMCO occurs in three stages, the first of which at 150 °C with weight loss of 4.0 and 7.0% for NCO and NMCO, respectively. This is owing to the removal of surface adsorbed water [32]. The second stage is from 160 to 250 °C with an average weight loss of 4.7 and 8.4% for NCO and NMCO, respectively, which can be related to the removal of internal adsorbed molecules of water. The third stage is from 300 to 00 °C with nearly weight loss of 6.2 and 11.3% for NCO and NMCO, respectively, which is related to the complete decomposition of residual organic compounds [33, 34]. Thermal degradation of MKCO occurs in three stages: the first stage at 120 °C with weight loss of 9.5% which is attributed to the removal of absorbed water. The second stage from 350 to 450 °C with weight loss of 21 and 25% is due to the decomposition of residual organic compounds, polymer chain, and carboxylate group destruction. Finally, the third stage occurs from 500 to 00 °C with weight loss of 25 and 38%, respectively, which is related to the formation of volatile carbonaceous compounds by the decomposition of organic molecules [32, 35].

Figure 1b represents nitrogen adsorption/desorption isotherms for all samples which are utilized for calculating the BET-specific surface area, pore radius, and total pore volume of NM, NCO, NMCO, and MKCO, as shown in Table 1. Based on the classification of IUPAC, the adsorption isotherms are classified as type IV for all samples while the hysteresis loops of type H2 for NM indicate monolayer of adsorption, while NCO, NMCO, and MKCO showed hysteresis loops of H3 type [6, 36–39]. The calculated specific surface areas were found to be 96.7, 348.0, 435.0, and 652.5 m²/g, respectively, while total pore volume values were 0.22, 0.26, 0.30, and 0.39 cm³/g for NM, NCO, NMCO, and MKCO, respectively. MKCO-specific surface area is more than that for NM and NCO by about 6.7 and 1.9 times, respectively. It is observed that increasing specific surface area is accompanied by increases in V_T (cm³/g) values which is related to the increase in porosity through modification of NCO and NM by potassium carrageenan [40]. The pore radii of NM, NCO, NMCO, and MKCO were 4.55, 2.12, 1.39, and 1.19 nm, respectively, indicating that all samples are mesoporous [9, 37–39]. The pore size of MKCO is less than NM and NCO by about 73.8 and 43.9%, respectively, which may be related to the effect of biopolymer potassium carrageenan insertion in NCO and NM pore structure during the composite formation [41].

SEM images were applied to evaluate the surface morphology of the synthesized NM, NCO, and MKCO as presented in Fig. 1c–e, respectively. NM appears as spherical globules with a rough and aggregated surface. The agglomeration of its structure is owing to its magnetic characteristics [9]. NCO appears as a homogenous circle-like morphology which may be related to the aggregation of particles during the preparation process, especially the washing step

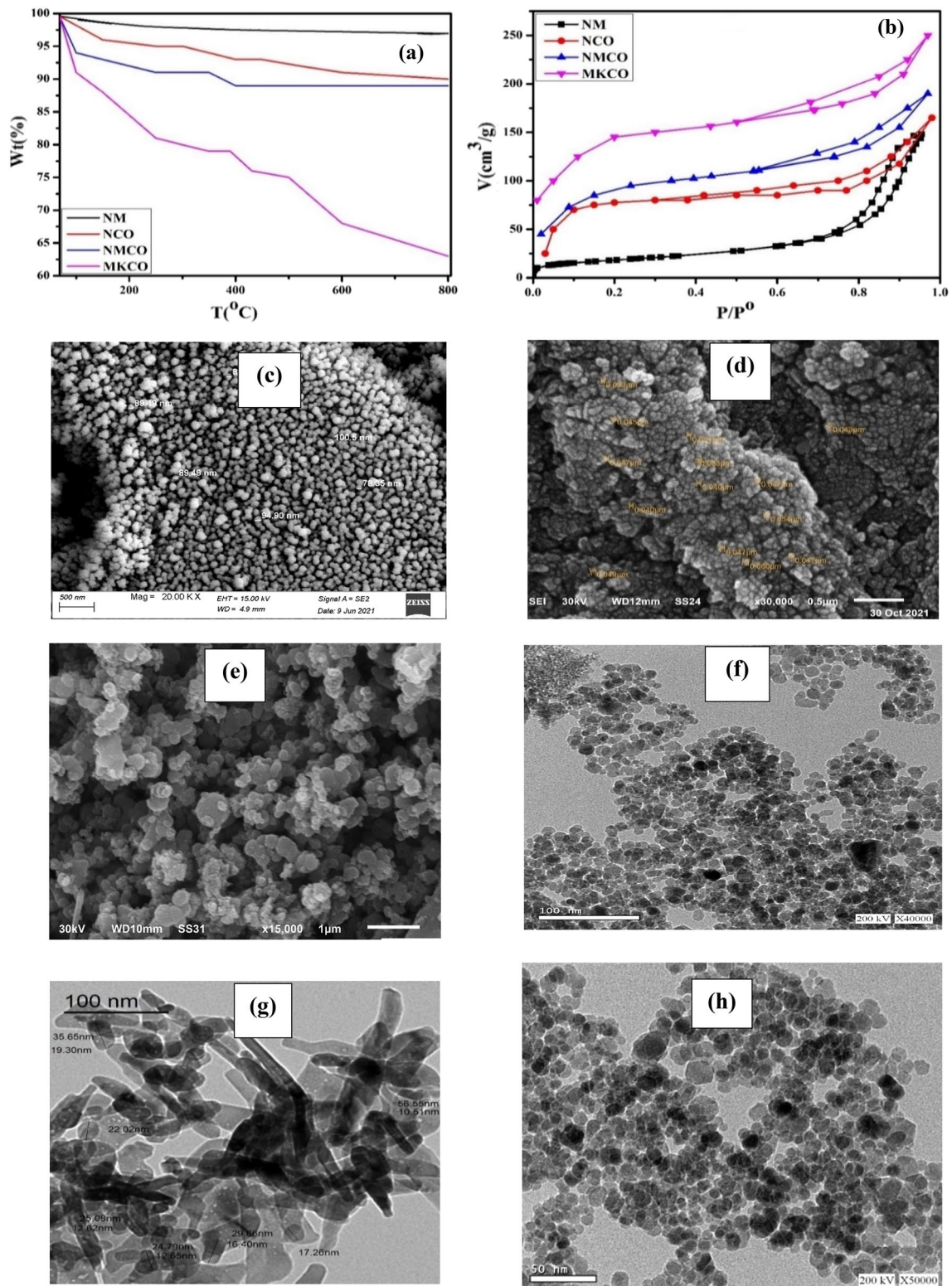


Fig. 1 TGA (a) and N₂ adsorption/desorption isotherms (b) for all the prepared solid samples, SEM (c–e), and TEM (f–h) for NM, NCO, and MKCO, respectively

Table 1 pH_{PZC} and BET parameters for NM, NCO, NMCO, and MKCO

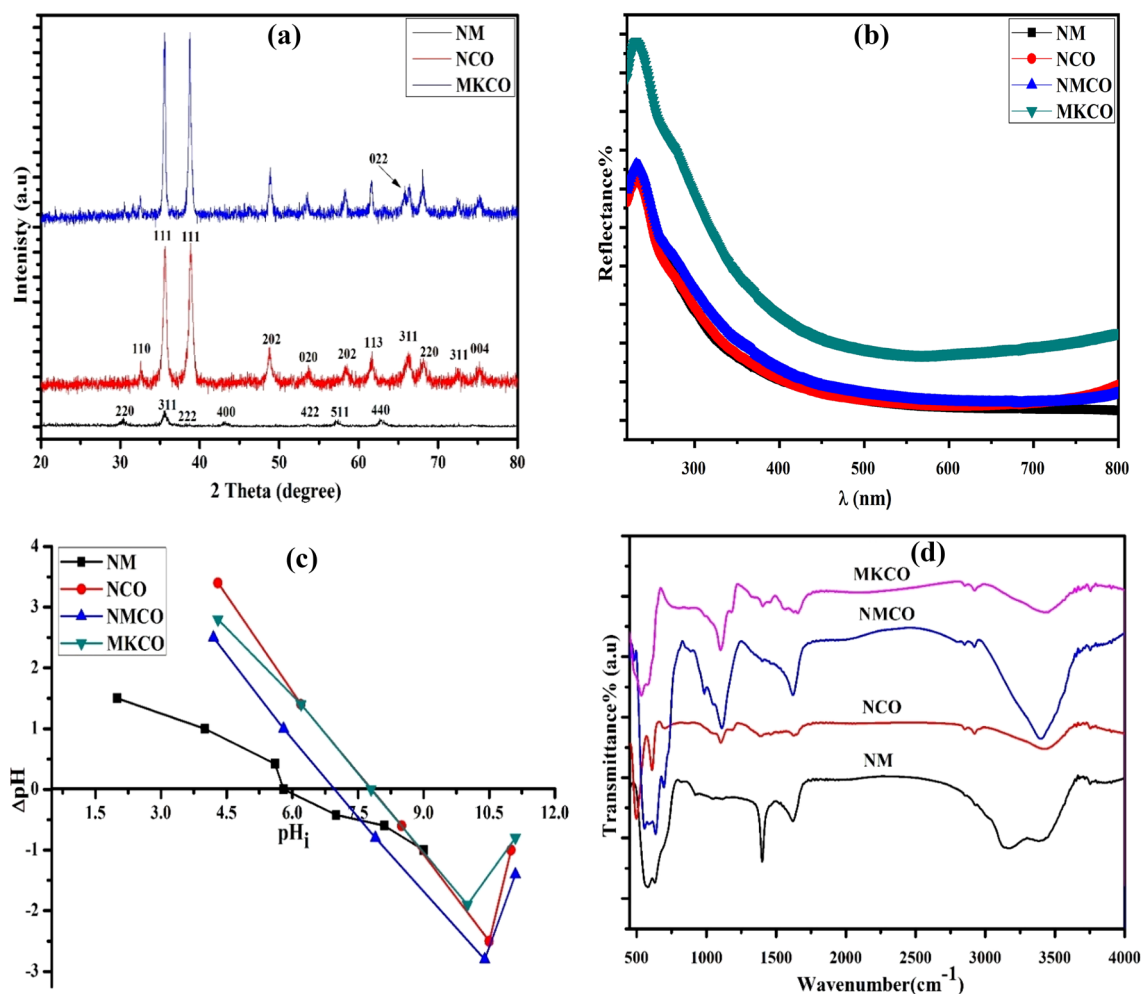
Solid samples	S_{BET} (m^2/g)	V_{T} (cm^3/g)	\bar{r} (nm)	pH_{PZC}
NM	96.7	0.22	4.55	5.80
NCO	348.0	0.26	2.12	8.70
NMCO	435.0	0.30	1.39	7.90
MKCO	652.5	0.39	1.19	7.80

[42]. SEM image for MKCO (Fig. 3e) showed spherical particles due to the incorporation of nanomagnetite and copper oxide in the matrix of potassium carrageenan biopolymer.

TEM micrographs of NM, NCO, and MKCO are presented in Fig. 1f–h, respectively. NM has a spherical appearance and homogenous shape with 5 nm as the average particle size, while NCO appears as a highly dispersed spindle and rod shape with particle sizes ranging from 10 to 100 nm

[10, 43]. MKCO exhibited spherical aggregated nanoparticles with nearly 150 nm as particle size.

The crystalline structures of the prepared NM, NCO, and MKCO are illustrated in Fig. 2a. XRD for NM was observed at 2θ degree of 30.3 (220), 35.6 (311), 38.3 (222), 43.5 (400), 53.4 (422), 57.6 (511), and 63.1° (440) which confirms the cubic structure of NM. As shown in Fig. 2a, the prepared NM is pure and crystalline owing to the absence of any peaks that cannot be identified [44, 45]. XRD for NCO and MKCO are identical, with highly crystalline peaks located at the same 2θ degree, except for the peak that appeared in XRD of MKCO at 2θ of 65.9° and can be matched with (022). This peak is related to the slight alteration in the structure of MKCO by K^+ ions doped in the carrageenan structure after modification of NCO by NC [46]. Average sizes of the crystals (P_s , nm) for NM, NCO, and MKCO can be calculated by the Debye–Scherer model (Eq. 31)

**Fig. 2** XRD (a) for NM, NCO, and MKCO, DRS (b), point of zero charges (c), and FTIR (d) for NM, NCO, NMCO, and MKCO

$$P_s(\text{nm}) = \frac{\lambda k}{\beta \cos \theta}, \quad (31)$$

where, λ is the wavelength of X-ray (0.15418 nm), $k=0.9$, β depicts the full width at half maximum of peaks, and the average particle size of NM, NCO, and MKCO was calculated to be 0.9, 0.4, and 1.9 nm, respectively [47].

The diffuse reflectance spectra (DRS) of NM, NCO, NMCO, and MKCO are displayed in Fig. 2b to investigate their optical properties and the following equation defines the semiconductor excitation wavelength (λ , nm) [29]:

$$\lambda(\text{nm}) = \frac{1240}{E_{\text{bg}}(\text{eV})}. \quad (32)$$

By applying the previous equation, energy band gaps (E_{bg} , eV) for NM, NCO, NMCO, and MKCO are found to be 2.90, 1.80, 1.78, and 1.76, respectively. The band-gap of MKCO < NMCO < NCO < NM is attributed to the increase in surface charges and chemical functional groups of NMCO, MKCO after modification of NCO by NM and NC, so the expected photocatalytic efficiency of MKCO > NMCO > NCO > NM owing to the reduction in their band gaps [40].

During the adsorption from solution at solid surface, the evaluation of pH_{PZC} is crucial. Table 1 lists the computed pH_{PZC} values from Fig. 2c curves, which were found to be in the range of 5.80–8.70 for all of the solid adsorbents [48, 49].

Chemical surface groups of NM, NCO, NMCO, and MKCO were determined by FTIR spectra. Figure 2d shows that for NM sample, the absorption band at 581 cm^{-1} is characteristic to NM and is specified to the stretching vibration frequency of Fe–O. The peak at 1621 cm^{-1} is related to (H–O–H) bending vibration owing to physisorbed water molecules at the surface of NM, while the peak located at 3382 cm^{-1} is referred to the stretching vibration of OH group. For NCO, the broadband that appeared at 3424 cm^{-1} is attributed to the stretching vibration of the hydroxyl group, the peak at 2923 cm^{-1} is due to the presence of a hydrogen bond. Peaks located at 425, 498, and 611 cm^{-1} are related to (Cu–O) stretching in the monoclinic phase of NCO. The spectrum of NMCO contains bands located at 557, 695, 2922, and 3398 cm^{-1} corresponding to Fe–O-stretching vibration of NM, Cu–O of NCO, hydrogen bond, and adsorbed water molecules (OH stretching), respectively, which confirm the formation of NMCO composite from NM and NCO. For MKCO spectrum peaks that displayed at 579, 2924, and 3426 cm^{-1} are attributed to Fe–O-stretching vibration of NM, a hydrogen bond, or the presence of C–H stretching in *k*-carrageenan, and OH-stretching vibration, respectively and that prove the nanocomposite formation (MKCO) between NM, NCO, and carrageenan biopolymer [36, 50, 51].

3.2 Adsorption of Safranin-O onto the prepared solid adsorbents

3.2.1 Effect of adsorbent dosage

Adsorbent dosage refers to the ratio between the proportion of adsorbate species and adsorbent active sites. NM and MKCO were selected to investigate the effect of adsorbent dosage from 0.06 to 2.0 g/L on the removal of SO. The selection of the two samples based on MKCO showed the maximum adsorption efficiency, while NM represents a single solid material component. As shown in Fig. 3a, increasing adsorbent dosage from 0.06 to 1.0 g/L leads to the enhancement in the removal (%) of SO from 24.8 to 50.7% for NM and from 31.9 to 85.0% for MKCO, which is related to the increase in the number of active sites and specific surface area of NM and MKCO with increasing their dosage [52, 53]. It is observed that, with increasing adsorbent dosage more than 1.0 g/L, the removal (%) sharply decreased to 36.3% at 2 g/L in case of NM which may be related to the agglomeration, adhesion of NM, and decreasing the ratio of active sites/SO dye molecules [9]. While in MKCO, the removal of SO remains almost constant, this is attributed to the establishment of adsorption equilibrium despite the occurrence of more surface active sites. The previous results confirm that 1.0 g/L of solid adsorbents is considered the best adsorbent dosage with the highest removal % of SO.

3.2.2 Effect of pH

The adsorption of SO dye is highly dependent on the solution pH which is responsible for the determination of the charge at the surface of adsorbate and adsorbent. The effect of pH on SO adsorption at the surface of NM and MKCO was studied at a pH range from 1 to 12 using 50 mL of 100 mg/L SO solution, 0.05 g of solid adsorbent (1.0 g/L as adsorbent dosage), and shaking time of 24 h at 25 °C (Fig. 3b). At reduced pH values ($\text{pH} < \text{pH}_{\text{PZC}}$), the surface of NM and MKCO acquires a positive charge and repelled the positively charged cationic dye (SO) beside the formation of H_3O^+ in the adsorbing medium which is responsible for lowering the removal percent of positive adsorbate by competition with the cationic SO dye molecules. At higher pH values, the removal (%) is increased with pH up to pH6 and pH8 by about 49.7 and 84.8% in the case of NM and MKCO, respectively. It is related to the fact that at $\text{pH} > \text{pH}_{\text{PZC}}$, solid adsorbents (NM and MKCO) acquire negative charges at their surface and lead to the increase in electrostatic attraction between SO (basic cation dye) and negatively charged adsorbents' surface [54, 55].

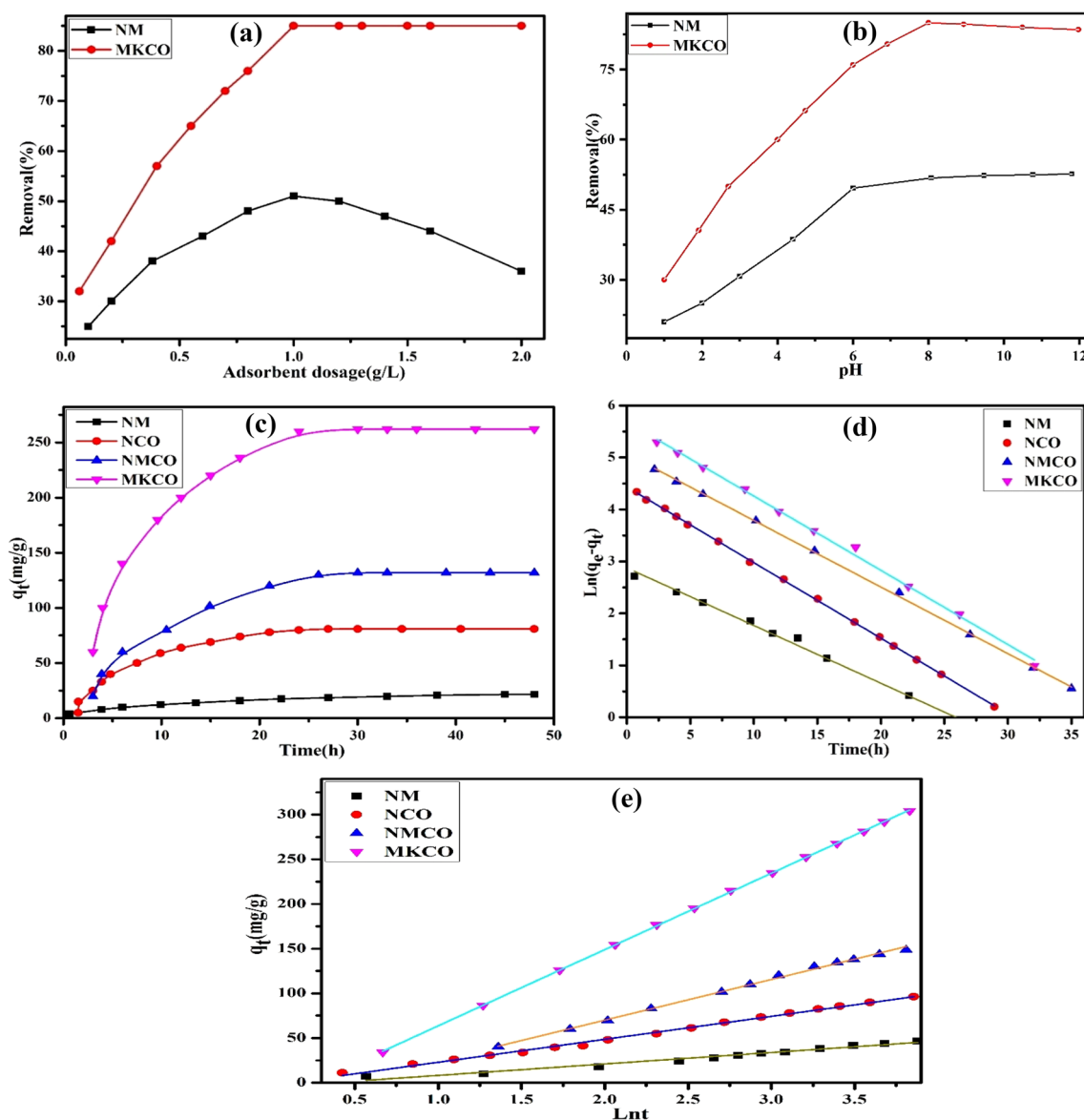


Fig. 3 Effect of adsorbent dosage (a), pH (b) on the adsorption of SO onto NM and MKCO, the effect of shaking time (c), PFO (d), and Elovich plots (e) for the adsorption of SO onto NM, NCO, NMCO, and MKCO at 25 °C

3.2.3 Effect of shaking time and kinetic parameters

In this study, adsorption rate has been investigated by applying pseudo-first-order (PFO, Eq. 20), pseudo-second-order (PSO, Eq. 21), and Elovich (Eq. 22) kinetic models for SO adsorption onto the surface of NM, NCO, NMCO, and MKCO after different periods up to 48 h using 50 mL of 100 mg/L SO, 1.0 g/L of solid adsorbent, pH7, and at 25 °C. Figure 3c depicts the adsorption capacities of all solid adsorbents against shaking time. At the beginning time up to 20 h for all solid samples, the rate of SO adsorption is higher, then the rate slowdown with time till reaches equilibrium (~24 h). The higher adsorption rate at

the beginning time is related to the rich of solid adsorbents surface with active sites, while the slowdown in adsorption rate is due to active sites' saturation with SO [27, 56]. PFO, Elovich, and PSO kinetic plots are shown in Fig. 3d, e, and Fig. 1Sa, respectively, while their calculated constants are tabulated in Table 2. Safranin-O adsorption was perfectly fitted by the PFO model due to the higher values of correlation coefficients ($R^2 > 0.9889$) for all investigated solid samples, in addition to the values of the calculated experimental adsorption capacity (q_{exp} , mg/g) for NM, NCO, NMCO, and MKCO (17.81, 84.22, 159.43, and 295.26) are very close to that values of the Langmuir adsorption model (q_m , mg/g) (16.91, 85.03, 164.70, and 284.90). R^2 values

Table 2 Pseudo-first-order, pseudo-second-order, Elovich kinetic models, and thermodynamic parameters for the adsorption of SO onto the surface of NM, NCO, NMCO, and MKCO at 25 °C

Solid samples	Parameters	NM	NCO	NMCO	MKCO	
PFO	q_m (mg/g)	16.91	85.03	164.70	284.90	
	q_e (mg/g)	17.81	84.22	159.43	295.26	
	k_1 (h ⁻¹)	0.1096	0.1456	0.1282	0.1429	
	R^2	0.9889	0.9996	0.9994	0.9973	
PSO	q_e (mg/g)	26.54	56.31	178.57	307.69	
	$k_2 \times 10^{-3}$ (g/mg h ⁻¹)	3.50	3.23	0.48	0.50	
	R^2	0.9963	0.9876	0.9872	0.9934	
Elovich	α (mg/g h ⁻¹)	8.92	23.01	28.59	66.13	
	β (g/mg)	0.078	0.039	0.022	0.012	
	R^2	0.9728	0.9959	0.9974	0.9999	
Parameters of thermodynamic	R^2	0.9946	0.9951	0.9999	0.9999	
	ΔH^0 (kJ mol ⁻¹)	5.521	10.528	6.041	5.063	
	ΔS^0 (kJ mol ⁻¹ K ⁻¹)	0.0203	0.0381	0.0226	0.0200	
	ΔG^0 (kJ mol ⁻¹)	25 °C	- 0.528	- 0.826	- 0.694	- 0.897
		32 °C	- 0.670	- 1.092	- 0.852	- 1.037
	42 °C	- 0.874	- 1.474	- 1.078	- 1.237	

calculated for adsorption of SO by PSO model are also high ($R^2 > 0.9872$), but the difference between q_{exp} and q_m (mg/g) values is very high (7.9–56.9%), confirming that PFO is the most appropriate method to study SO adsorption rather than PSO kinetic model. The accepted PFO model indicates that the physisorption mechanism is the dominant mechanism for SO adsorption. Elovich's kinetic model is fitted for the SO adsorption process owing to the higher R^2 values for all solid adsorbents (> 0.9728). β and α values are located in the ranges of 0.012–0.078 g/mg and 8.92–66.13 mg/g h⁻¹, respectively, and indicate that the equilibrium of adsorption and surface coverage for all solid adsorbents are confirmed in a very short time [57, 58].

3.2.4 Effect of Safranin-O initial concentration

Figure 4a represents the adsorption isotherms for adsorption of SO onto NM, NCO, NMCO, and MKCO at different temperatures (25, 32, and 42 °C), considering the initial concentration of SO (5–650 mg/L), the adsorbent dosage of 0.05 g, pH7, and 24 h of shaking time. The data obtained from the produced adsorption isotherms were calculated by the analysis of Eqs. (12, 14, 15, and 17). Figure 4a shows that the adsorption of SO ions is high at a lower initial concentration which may be attributed to the increase in active sites ratio to the number of SO ions and decreased with increasing that ratio at a higher initial concentration of SO ions [56]. Figure 4b–e depicts the Langmuir adsorption model onto NM, NCO, NMCO, and MKCO, respectively, while the calculated parameters of Langmuir are listed in Table 3. Langmuir model is well applied due to the higher values of R^2 (0.9888–0.9989), and the calculated q_m (mg/g) for NM, NCO, NMCO, and MKCO were found to be 27.45,

112.23, 185.87, and 384.61 mg/g at 42 °C, respectively, indicating that modification of NCO by NM and NC increases the adsorption capacities of modified solid adsorbents (MKCO > NMCO > NCO > NM). Langmuir adsorption capacity (q_m , mg/g) values of NMCO and MKCO are more than NM and NCO, which is due to increasing total pore volume, specific surface area, and the addition of new chemical functional groups originated from the incorporation of carrageenan in the case of MKCO at the surface of modified adsorbents. The calculated values of R_L (0.040–0.403) are less than unite and indicate the favorable adsorption process onto the surface of NM, NCO, NMCO, and MKCO. Freundlich adsorption plots are shown in Fig. 1Sb–e and their calculated parameters are illustrated in Table 3. The calculated Freundlich R^2 values were found to be 0.9619–0.9881 for the adsorption of SO onto all the studied solid adsorbents. The calculated $1/n$ values are less than 1 and ranged from 0.131 to 0.877, which are classified as L-type isotherms confirming a high affinity between adsorbents and SO. The values of K_F are used to determine adsorption capacity and increasing K_F (L/mg) values (1.53–161.71) with the increase in temperature indicate that adsorption of SO is endothermic [58–60]. The calculated Langmuir correlation coefficient values (0.9888–0.9989) are higher than that calculated from Freundlich models (0.9619–0.9881), proving that the Langmuir model well fits the adsorption of SO onto all the investigated solid adsorbents. Figure 2Sa–d predicts Temkin adsorption plots for adsorption of SO onto NM, NCO, NMCO, and MKCO, respectively, while Temkin parameters are tabulated in Table 3. Adsorption data of SO by all solid adsorbents are perfectly fitted by the Temkin model as shown in the higher values of R^2 (0.9779–0.9997). The values of K_T (L/g) increase with temperature increase

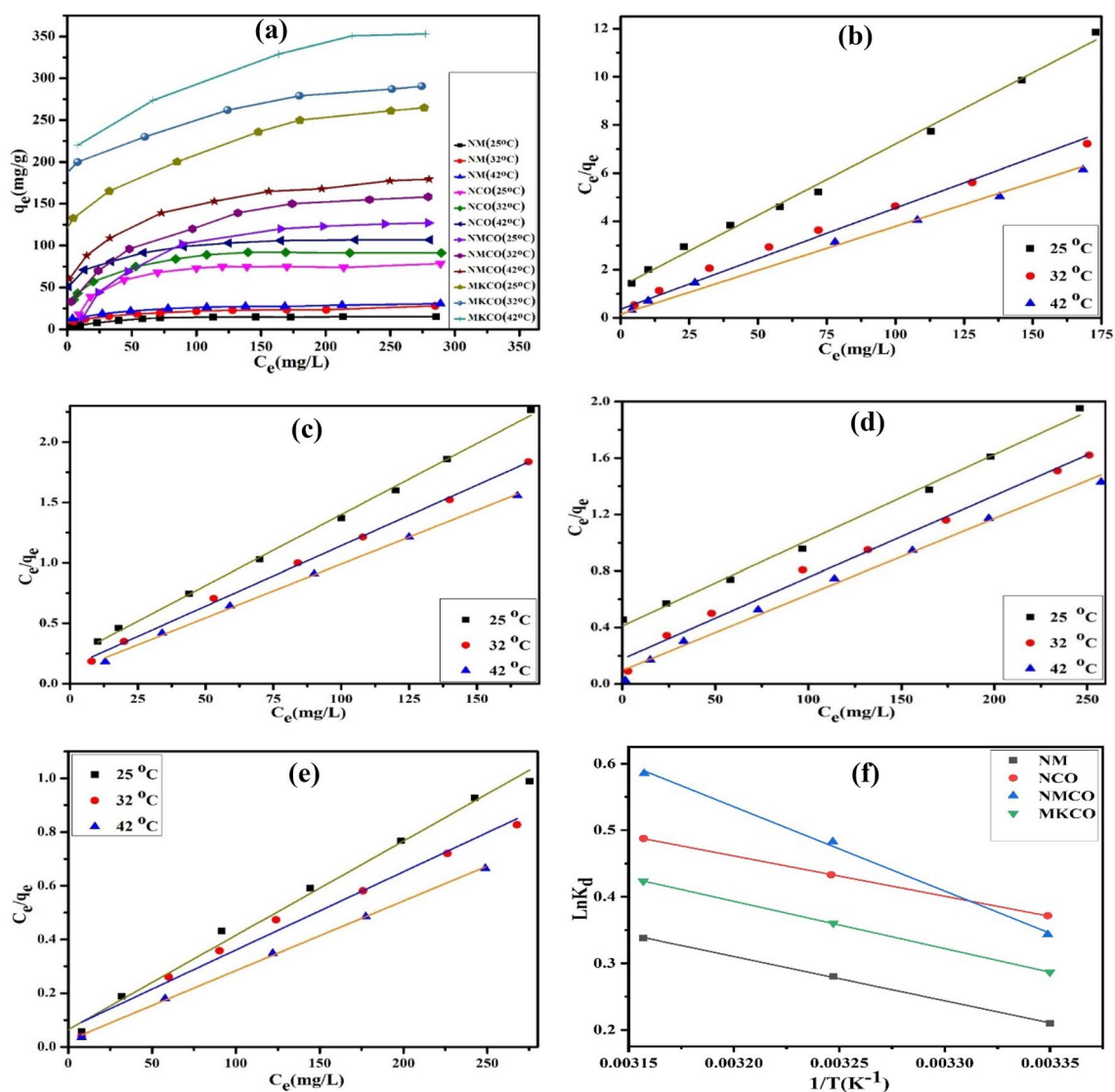


Fig. 4 Adsorption isotherms (a), Langmuir (b–e), and Van't Hoff plots (f) for the adsorption of SO onto NM, NCO, NMCO, and MKCO, respectively at 25, 32, and 42 °C

for all prepared solid adsorbents which confirms the process is endothermic and the higher K_T values for NMCO and MKCO samples indicate that the binding force between SO dye and the solid surface is stronger. The values of the Temkin parameter (b_T , J/mol) for NM, NCO, NMCO, and MKCO at different temperatures located between 59.26 and 697.01 J/mol, ($b_T < 8000$ J/mol) indicate the dominance of physical adsorption [61]. Dubinin–Radushkevich model (DR) for SO adsorption onto NM, NCO, NMCO, and MKCO is represented in Fig. 3Sa–d and the calculated parameters of the model are listed in Table 3. The calculated R^2 values of the DR model's different applied temperatures are more than 0.9528. The difference between calculated q_{DR} (mg/g) and (q_m , mg/g) from the Langmuir model ranged between 0.35 and 17.03% for all the solid adsorbents. The

previous observations confirm that the DR adsorption model is perfectly applied for SO adsorption. The calculated E_{DR} (kJ/mol) values are less than 8.0 kJ/mol as indicated in Table 3 which proves the physical adsorption of SO onto the studied solid samples [27, 62].

3.2.5 Effect of temperature and thermodynamic parameters

Adsorption of SO was studied on NM, NCO, NMCO, and MKCO at 25, 32, and 42 °C using 0.05 g as adsorbent dosage, 24 h of shaking time, pH7, and different initial concentrations of dye. Thermodynamic parameters were calculated by the application of Eqs. 24–26, as presented in Van't Hoff plot (Fig. 4f). Upon analysis of thermodynamic data

Table 3 Langmuir, Freundlich, Temkin, and Dubinin–Radushkevich parameters for the adsorption of SO onto NM, NCO, NMCO, and MKCO at 25, 32, and 42 °C

Parameters	NM			NCO			NMCO			MKCO		
	25 °C	32 °C	42 °C	25 °C	32 °C	42 °C	25 °C	32 °C	42 °C	25 °C	32 °C	42 °C
Langmuir model												
q_m (mg/g)	16.91	23.38	27.45	85.03	99.90	112.23	164.70	173.01	185.87	284.90	343.64	384.61
b (L/mg)	0.045	0.117	0.243	0.053	0.071	0.089	0.015	0.032	0.057	0.054	0.042	0.108
R_L	0.182	0.077	0.040	0.159	0.124	0.101	0.403	0.234	0.149	0.156	0.192	0.085
R^2	0.9952	0.9888	0.9989	0.9984	0.9983	0.9984	0.9949	0.9891	0.9914	0.9932	0.9935	0.9989
Freundlich model												
1/n	0.269	0.228	0.502	0.559	0.295	0.160	0.877	0.376	0.214	0.187	0.131	0.146
K_F (L/mg)	6.14	8.84	1.53	6.12	23.03	50.96	1.89	23.15	56.27	93.94	149.70	161.71
R^2	0.9852	0.9827	0.9880	0.9619	0.9793	0.9881	0.9726	0.9823	0.9881	0.9791	0.9719	0.9880
Temkin model												
b_T (J/mol)	697.01	599.72	604.10	117.58	148.69	240.24	59.26	86.60	114.32	69.81	70.82	61.07
K_T (L/g)	0.52	1.59	3.82	0.30	1.51	88.99	0.12	0.87	6.78	6.19	21.69	21.72
R^2	0.9937	0.9924	0.9914	0.9872	0.9989	0.9895	0.9991	0.9904	0.9779	0.9982	0.9885	0.9997
Dubinin–Radushkevich model												
q_{DR} (mg/g)	14.03	18.37	21.01	68.05	75.98	97.46	121.21	153.01	164.66	285.90	337.68	391.34
E_{DR} (kJ/mol)	0.198	0.402	0.282	0.104	0.233	1.176	0.051	0.066	0.124	0.050	0.038	0.033
R^2	0.9977	0.9863	0.9948	0.9653	0.9915	0.9989	0.9883	0.9968	0.9873	0.9959	0.9528	0.9694

in Table 2, (i) the higher values of $R^2 > 0.9946$ for Fig. 4f indicate the well-fitting of Van't Hoff plot. (ii) Values of ΔS° are positive for the adsorption process onto all the solid adsorbents confirming the increase in the randomness of SO at the surface of adsorbents during the adsorption. (iii) ΔH° values are ranged between 5.063 and 10.528 kJ/mol which indicates that adsorption of SO is endothermic and proves the increase in q_{max} (mg/g) for all the solids (NM, NCO, NMCO, and MKCO) with temperature. ΔH° values < 25 kJ/mol, which shows that Vander Waals interactions are the dominant force and indicates the physical adsorption of SO at the surface of adsorbents. (iv) The values of ΔG° are negative (0.528–1.474 kJ/mol) for NM, NCO, NMCO, and MKCO confirming the spontaneous and favorable adsorption process of SO dye [63].

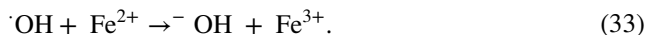
3.3 Degradation of Safranin-O using heterogeneous Fenton process

Safranin-O degradation using the heterogeneous Fenton process is investigated through various parameters like the effect of catalyst dosage, the effect of pH, hydrogen peroxide concentration, initial concentration of SO, UV illumination, and the effect of applied temperature.

3.3.1 Catalyst dosage effect

Figure 5a illustrates the dosage effect of NM on SO degradation with time using dosage mass up to 2.0 g/L, using

10 mg/L of SO as initial dye concentration, 50 mmol of H_2O_2 , pH3, and at 21 °C. It is observed that with the increase in NM catalyst dosage to 1.0 g/L, the oxidation of SO also increases, but at a dosage of more than 1.0 g/L, degradation starts to decrease. The enhancement in SO degradation with increasing NM dosage from 0.8 to 1.0 g/L is attributed to the increase in the number of catalytically active sites with the increase in NM dosage, leading to the increase in SO degradation through a rise in the quantity of Fe^{2+} that interact with H_2O_2 to form $\cdot OH$, as shown in Eq. 1. Degradation (%) of SO decreases at catalyst dosages > 1.0 g/L is related to the scavenging of Fe^{2+} ions on $\cdot OH$ as indicated in Eq. 33. As a result, a catalyst dosage of 1.0 g/L is considered to be the ideal dosage for Fenton degradation of SO [64]



3.3.2 pH effect on Safranin-O degradation

The influence of pH on the oxidation of SO was investigated using a pH range of (2.2–6.0), 10 mg/L SO, 1.0 g/L of NM as solid dosage, and 50 mmol H_2O_2 at 21 °C (Fig. 5b). After 60 min, the degradation (%) of SO was calculated to be 45.78, 56.15, 36.41, and 34.13% at pH 2.2, 3.0, 4.3, and 6.0, respectively. It is obvious that with pH increase till pH3, the degradation (%) of SO increases, and further increases in the values of pH lead to the decrease in degradation efficiency of SO. Lower

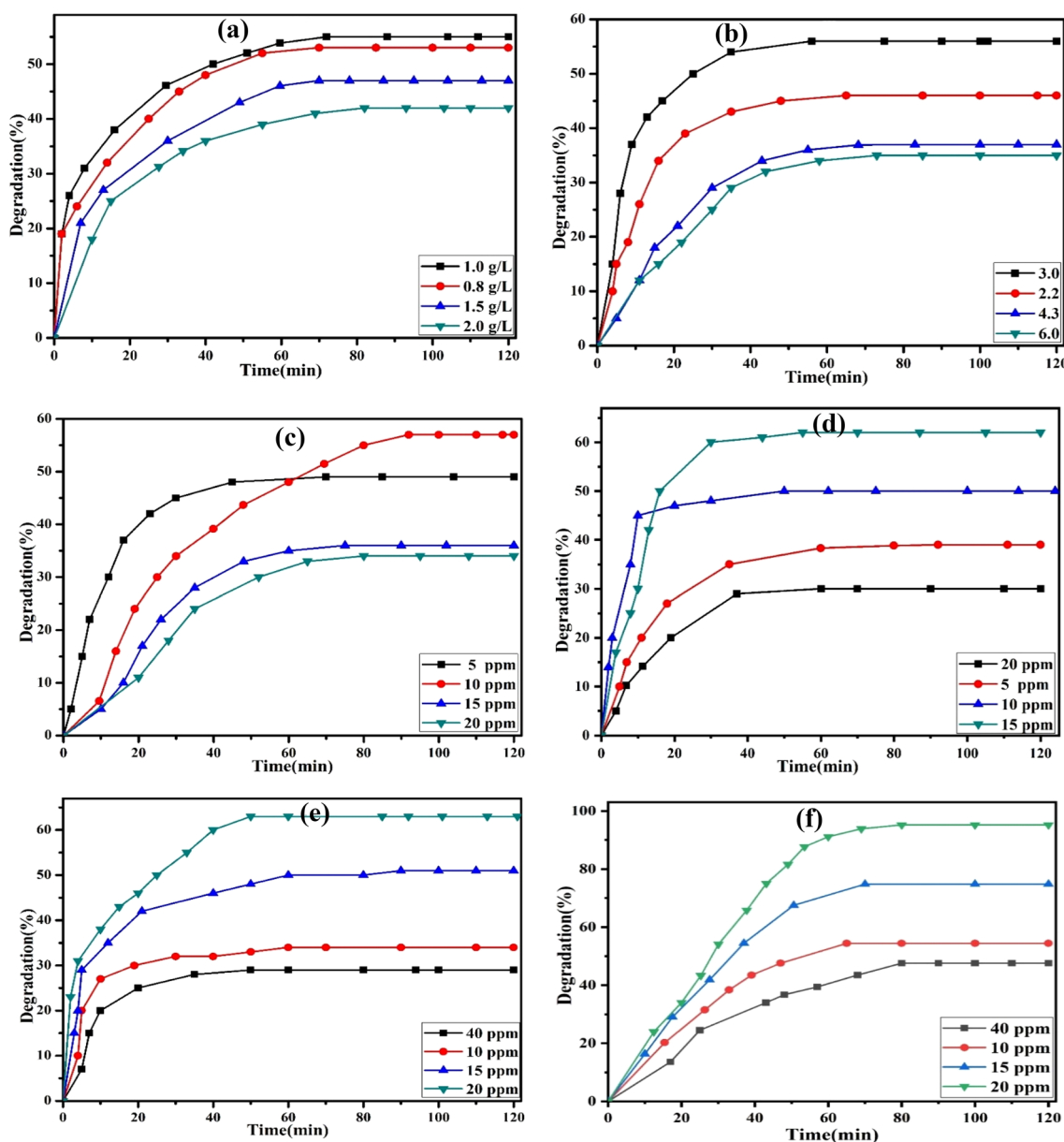
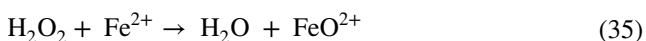


Fig. 5 Effect of NM catalyst dosage (a), the effect of pH (b) using NM, and the effect of initial concentration of SO (c–f) by NM, NCO, NMCO, and MKCO, respectively, on the degradation of Safranin-O via heterogeneous Fenton process at 21 °C

SO degradation at lower values of pH is attributed to $\cdot\text{OH}$ conversion into H_2O and the production of inactive FeO^{2+} , and the conversion of H_2O_2 into stable oxonium ion (H_3O_2^+) by the protonation with H^+ , as shown in Eqs. (34–36)



At higher pH values, SO degradation (%) decreases owing to the formation of oxygen and water by decomposition of H_2O_2 and the formation of iron hydroxide instead of $\cdot\text{OH}$ by Fe (II). These previous results confirm that pH3 shows the maximum oxidation efficiency [65–67].

3.3.3 Effect of Safranin-O initial concentration

The effect of initial Safranin-O concentration by varying its concentration from 5 to 20 mg/L for NM and NCO and from 10 to 40 mg/L in case of NMCO and MKCO, respectively, 50 mmol of H_2O_2 concentration, pH3, 1.0 g/L as catalyst

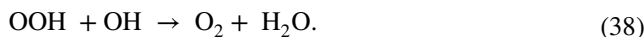
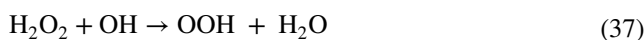
dosage, at 21 °C are shown in Fig. 5c–f. After 80 min of Fenton SO oxidation, the maximum degradation percent was found to be 55, 62, 64, and 96% (at 10, 15, 20, and 20 ppm) using NM, NCO, NMCO, and MKCO, respectively. That means that NMCO and MKCO showed a very higher catalytic Fenton oxidation process for the dye (64 and 96%, respectively) at a higher concentration of SO (20 mg/L) compared with the other two catalysts (NM and NCO). The previous result confirms that the involvement of NCO and NM in the formation of new composites (NMCO) enhanced the degradation (%) of SO due to the role of Cu^+ in the oxidation process as indicated in Eqs. 4,5. On the other hand, MKCO exhibited a higher oxidation efficiency which may be related to the good distribution of Fe (II) and Cu (I) on the solid surface formulated by *k*-carrageenan, the reduction in E_a (activation energy) needed for the degradation of SO, and the good fixation of SO ions onto the surface of composites.

Regarding the effect of initial dye concentrations, it is observed that at the first stages of increasing concentration, the degradation % by the heterogeneous Fenton oxidation process is enhanced due to the higher collisions between SO molecules and the produced active species. Excessive increase in the initial concentrations of more than 10, 15, 20, and 20 mg/L in case of NM, NCO, NMCO, and MKCO, respectively, leads to an observable decrease in the percentage of SO degradation which is owing to the increase in the ratio of oxidizing species to SO molecules [68]. The previous section showed that 10, 15, 20, and 20 mg/L are the most suitable initial Safranin-O concentration for the Fenton degradation process using NM, NCO, NMCO, and MKCO, respectively.

3.3.4 Hydrogen peroxide effect

Hydrogen peroxide is the primary source of active $\cdot\text{OH}$ and is the catalyst for SO degradation in the heterogeneous Fenton process. Figure 6a represents the effect of hydrogen peroxide concentration from 30 to 100 mmol, using 10 mg/L of SO initial concentration, 1.0 g/L of NM dosage, pH3, at 21 °C. Degradation of SO after 80 min reached about 50, 56, 45, and 39% in the presence of 30, 50, 75, and 100 mmol of hydrogen peroxide, respectively. It is noted that with increasing H_2O_2 up to 50 mmol, the degradation of SO also increases and then decreases till reaches 39% in the presence of 100 mmol hydrogen peroxide. The enhancement of degradation efficiency at the beginning with hydrogen peroxide concentration is owing to the increase in $\cdot\text{OH}$ as oxidizing species, while the observed decrease at concentrations > 50 mmol is explained by the scavenging of $\cdot\text{OH}$ and the conversion into less active species, as shown in Eqs. (37, 38). This is accompanied by alteration in heterogeneous Fenton mechanism; as a result, 50 mmol is considered the

optimum hydrogen peroxide concentration in the heterogeneous Fenton process [69]



3.4 Degradation of Safranin-O by Photo-Fenton process

3.4.1 UV illumination effect on Safranin-O degradation

Photo-Fenton degradation of SO was studied by carrying out six experiments: (i) 100 mL of 10 mg/L of SO solution was exposed to photolysis (UV light, 254 nm). (ii) 100 mL SO solution with a concentration of 10 mg/L, 50 mmol of H_2O_2 , and UV radiation. (iii) 100 mL SO solution with a concentration of 10 mg/L, 50 mmol of H_2O_2 , and 0.1 g of NM catalyst under UV radiation. (iv) 100 mL of 10 mg/L of SO solution, 50 mmol of H_2O_2 , and 0.1 g of NCO catalyst under UV illumination. (v) 100 mL of SO solution with a concentration of 10 mg/L, 50 mmol of H_2O_2 , and 0.1 g of NMCO catalyst under UV illumination. (vi) 100 mL SO solution with a concentration of 10 mg/L of SO solution, 50 mmol of H_2O_2 , and 0.1 g of MKCO catalyst under UV illumination. All the previous experiments were applied at pH3 and 21 °C. Degradation of SO by Photolysis and Photo-Fenton are shown in Fig. 6b. After 10 min, SO degradation was calculated to be 13, 30, 70, 79, 85, and 93% for Photolysis in the absence and the presence of hydrogen peroxide, and Photo-Fenton degradation in the presence of NM, NCO, NMCO, and MKCO, respectively. It is noted that the degradation efficiency of SO increases from 13 to 32 in the second experiment (Photolysis) due to the inclusion of hydrogen peroxide in the reaction, which is attributed to the release of $\cdot\text{OH}$ responsible for the degradation of SO molecules [10]. Photo-Fenton experiments (iii, iv, v, vi) using NM, NCO, NMCO, and MKCO as solid catalysts exhibited degradation percent of $\text{MKCO} > \text{NMCO} > \text{NCO} > \text{NM}$, which may be owing to the higher porosity, specific surface area, incorporation of Cu^+ with Fe^{+2} , the presence of more polar chemical groups created from modification of NCO by NM and NC, and the perfect distribution of ferrous and cuprous ions at the surface of NMCO and MKCO nanoparticles. Comparing between Fenton and Photo-Fenton oxidation of the dye in presence of NM, NCO, NMCO, and MKCO after 10 min under the same condition (Figs. 5c–f and 6b) of oxidation, we observed the higher efficiency of the Photo-Fenton process by nearly about 11, 4, 3, and 5 times than Fenton degradation process for NM, NCO, NMCO, and MKCO, respectively. In summary, the enhancement of the

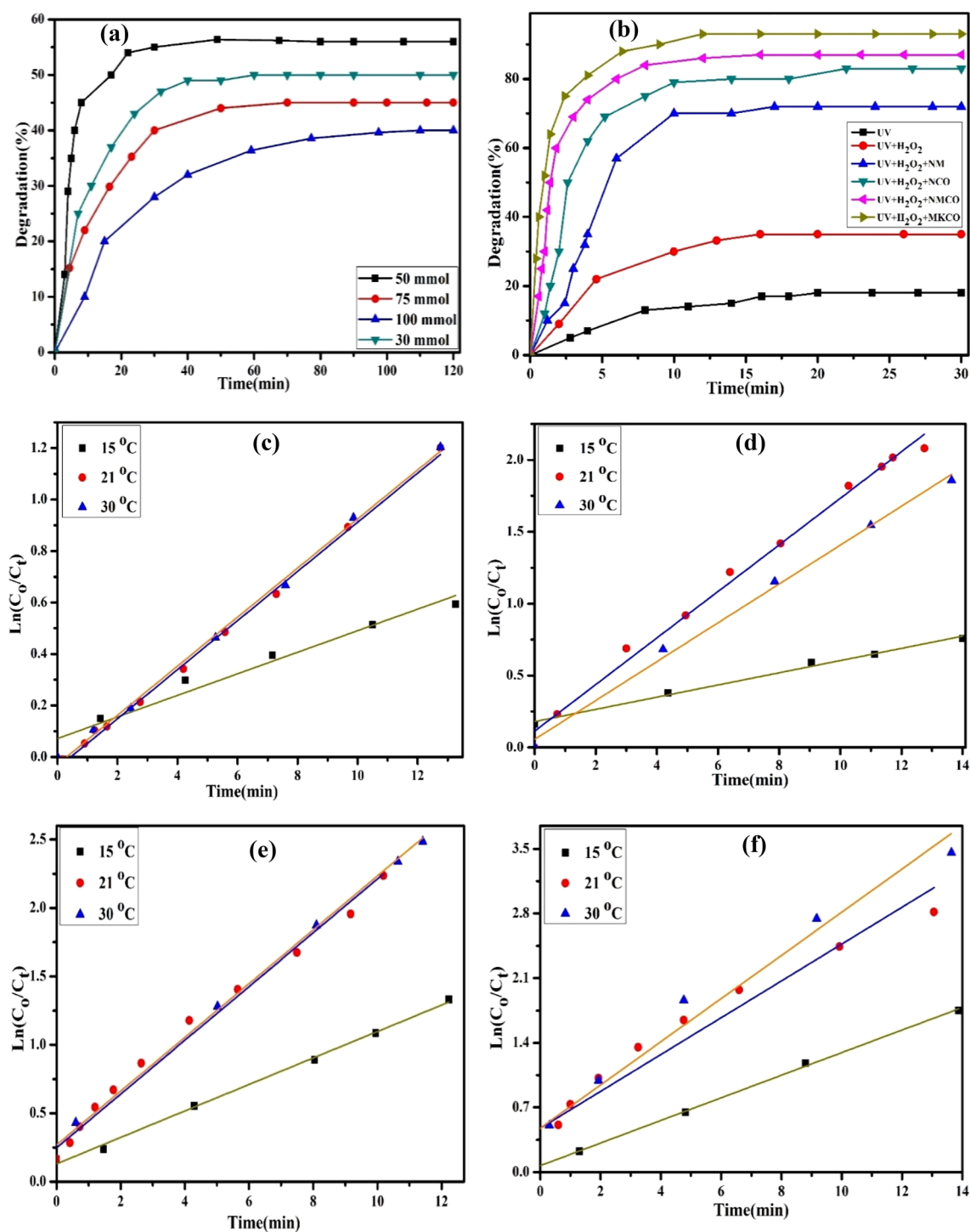
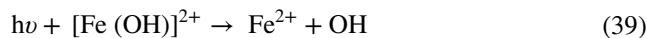


Fig. 6 Effect of hydrogen peroxide concentrations (a) using NM for Safranin-O degradation by Fenton process. Photo-Fenton studies (b) using NM, NCO, NMCO, and MKCO, and kinetic plots (c–f) for NM, NCO, NMCO, and MKCO, respectively

degradation under the Photo-Fenton process is attributed to the production of $\cdot\text{OH}$ owing to the effect of UV radiation on hydrogen peroxide and Fe^{3+} ions which is reduced to active Fe^{2+} at the applied value of pH as shown in Eqs. (39,40) [70, 71]



3.4.2 Kinetic parameters of SO degradation by Photo-Fenton process

The kinetic study of SO degradation was investigated by the application of Eq. 27 at different temperatures (15, 21, and 30 °C) as represented in Fig. 6c–f for NM, NCO, NMCO, MKCO, respectively, and the obtained kinetic parameters are listed in Table 4. The values of R^2 for NM, NCO, NMCO, and MKCO are more than 0.9717, confirming that the Photo-Fenton degradation for all solids follows the model of PFO kinetic. Throughout the applied temperatures, the calculated K_{app} (min^{-1}) for MKCO > NMCO > NCO > NM is attributed to the activity of MKCO > NMCO > NCO > NM as presented in the previous sections (Sect. 3.4.1). The values of K_{app} (min^{-1}) increase with increasing temperature for all solids and that is related to the increase in reaction rate with the increase in temperature [72].

3.4.3 Effect of temperature on Photo-Fenton degradation of Safranin-O

The effect of applied temperature on the oxidation of SO by the Photo-Fenton process is illustrated in Fig. 4Sa–d for NM, NCO, NMCO, and MKCO, respectively, using 100 mL of 0.1 g solid dosage, pH3, 10 mg/L of SO solution as initial concentration, 50 mmol of H_2O_2 at different temperatures (15, 21, and 30 °C). It is observed that with rising temperature, the degradation of SO also increases which may be explained by the increase in the production of hydroxyl radical and the reaction rate between catalysts and hydrogen peroxide, confirming that degradation of SO is endothermic [72]. The values of E_a (kJ/mol) and all thermodynamic parameters for degradation of SO using NM, NCO, NMCO, and MKCO catalysts were determined by Eqs. (28–30), as shown in Fig. 4Se, f, while the calculated parameters are

displayed in Table 4. Upon inspection of data, Table 4, (i) according to the higher R^2 values, confirms the good application of Arrhenius (> 0.9706) and Eyring-Polanyi (> 0.9784) models (Eqs. 28, 29, respectively). (ii) The calculated values of E_a (kJ/mol) in Photo-Fenton degradation of SO in the presence of NM, NCO, NMCO, and MKCO catalysts are more than 20 kJ/mol indicating the chemical nature of the degradation process. (iii) The values of ΔH^* (kJ/mol) are positive which indicates that Photo-Fenton degradation of SO is endothermic [73]. (iv) ΔS^* ($\text{kJ mol}^{-1} \text{K}^{-1}$) values were calculated to be negative 0.046 and 0.043 for NM and NCO, respectively, positive 0.030 and 0.037 for NMCO and MKCO, respectively. The negative values of ΔS^* are explained by the decreases in SO randomness at the solid surface of NM and NCO which indicate an irreversible tendency for the process, while the positive values are due to the increasing randomness of SO at the surface of NMCO and MKCO. (v) The values of ΔG^* (kJ/mol) are positive, proving that the SO degradation process is non-spontaneous [30, 74].

3.4.4 Reusability of catalyst

The reusability of MKCO as a selected catalyst for degradation of SO by the Photo-Fenton process was assessed after five application cycles as represented in Fig. 5S. After five cycles, it was observed that the catalytic activity of MKCO reduced by about 3.4% which may be due to the slight decrease in specific surface area, loss of some active sites, and porosity of MKCO as a result of its coagulation [4].

3.5 Comparison between MKCO with other solids

In the present work, a comparison between MKCO with other different solids for Photo-Fenton degradation and

Table 4 Kinetic and thermodynamic parameters of SO by Photo-Fenton using NM, NCO, NMCO, and MKCO photocatalysts at 15, 21, and 30 °C using 10 mg/L of SO, 50 mmol of H_2O_2 , and 0.1 g of catalyst

Nanocatalyst	NM			NCO			NMCO			MKCO		
	15 °C	21 °C	30 °C	15 °C	21 °C	30 °C	15 °C	21 °C	30 °C	15 °C	21 °C	30 °C
Kinetic parameters												
K_{app} (min^{-1})	0.0419	0.0953	0.0954	0.0424	0.1351	0.1619	0.0967	0.1964	0.1965	0.1223	0.1994	0.2338
R^2	0.9717	0.9965	0.9975	0.9907	0.9939	0.9918	0.9966	0.9861	0.9964	0.9990	0.9765	0.9749
Thermodynamic parameters												
E_a (kJ/mol)		32.36			34.11			56.65			58.91	
A		11.42			11.92			20.53			21.40	
R^2		0.9968			0.9960			0.9706			0.9925	
ΔS^* ($\text{kJ mol}^{-1} \text{K}^{-1}$)		– 0.046			– 0.043			0.030			0.037	
ΔH^* (kJ/mol)		34.86			36.47			59.31			61.44	
R^2		0.9784			0.9999			0.9872			0.9847	
ΔG^* (kJ/mol)	48.11	48.38	48.80	48.85	49.11	49.50	50.67	50.49	50.22	50.78	50.56	50.23

adsorption of SO is shown in Table 6S [75–80]. According to the data listed in Table 6S, it is observed that MKCO is a promising solid material for both Photo-Fenton catalytic degradation and adsorption of Safranin-O dye. Regarding the present material and other materials in comparison table, we can note that adsorption is applied for higher pollutant concentration at higher equilibrium time, while Photo-Fenton catalytic degradation is used for lower pollutant concentration with very short application time compared with the adsorption process.

3.6 Conclusion

This work effectively manufactured a new solid composite material made of copper oxide, potassium carrageenan, and nanomagnetite particles. The prepared solid nanomaterials were characterized using different physicochemical techniques, such as TGA, SEM, TEM, DRS, N₂ adsorption/desorption isotherm, pH_{PZC}, and FTIR. The nanomagnetite/copper oxide/potassium carrageenan composite nanoparticles (MKCO) demonstrated a well-structured porous material for the distribution of both Fe⁺² and Cu⁺, higher specific surface area (652.50 m²/g), pore radius of 1.19 nm, point of zero charge at pH7.8, Debye-Scherrer particle size of about 1.9, and the rich with numerous chemical polar functional groups. SEM and TEM investigation of MKCO showed that the measured particle size ~ 150 nm with spherical aggregated shapes. Safranin-O (SO) dye adsorption and Photo-Fenton degradation were compared using all the produced materials in various application scenarios. MKCO showed the maximum adsorption capacity of 384.61 at 42 °C after 24 h of equilibrium time, and at a higher initial concentration of the dye (5–650 mg/L). Photo-Fenton degradation of SO dye was well performed on the surface of MKCO with about 93% degradation after 10 min using lower SO concentration (10 mg/L), and at 21 °C. Catalyst reusability during Photo-Fenton process confirmed the successful uses of catalyst even after five cycles of application with only 3.4% decrease in catalytic activity. The effectiveness of the prepared materials for use in environmental applications is increased by the newly developed solid materials that integrate a kappa-carrageenan biopolymer matrix. The earlier findings support the potential environmental benefits of MKCO nanoparticles in Photo-Fenton degradation and dye adsorption at both high and low levels of pollution.

Supplementary Information The online version contains supplementary material available at <https://doi.org/10.1007/s13233-023-00147-4>.

Author contributions AFH and LMA: supervision, conceptualization, writing—review, methodology, and editing. AMA, AAM, and GE: methodology, software, data curation, and writing—original draft.

Funding Open access funding provided by The Science, Technology & Innovation Funding Authority (STDF) in cooperation with The Egyptian Knowledge Bank (EKB).

Declarations

Conflict of interest The authors declare that they have no known competing financial interests or personal relationships that could have appeared to influence the work reported in this paper.

Open Access This article is licensed under a Creative Commons Attribution 4.0 International License, which permits use, sharing, adaptation, distribution and reproduction in any medium or format, as long as you give appropriate credit to the original author(s) and the source, provide a link to the Creative Commons licence, and indicate if changes were made. The images or other third party material in this article are included in the article's Creative Commons licence, unless indicated otherwise in a credit line to the material. If material is not included in the article's Creative Commons licence and your intended use is not permitted by statutory regulation or exceeds the permitted use, you will need to obtain permission directly from the copyright holder. To view a copy of this licence, visit <http://creativecommons.org/licenses/by/4.0/>.

References

- H. Xue, X. Gao, M.K. Seliem, M. Mobarak, R. Dong, X. Wang, K. Fu, Q. Li, Z. Lim, Efficient adsorption of anionic azo dyes on porous heterostructured MXene/ biomass activated carbon composites: experiments, characterization, and theoretical analysis via advanced statistical physics models. *Chem. Eng. J.* **451**, 138735 (2023). <https://doi.org/10.1016/j.cej.2022.138735>
- M. Umar, C.C. Nnadike, I. Abdulazeez, K. Alhooshani, A.A. Al-Saadi, Nitrogen-enhanced charge transfer efficacy on the carbon sheet: a theoretical insight into the adsorption of anionic dyes. *Arab. J. Sci. Eng.* **47**, 419–427 (2022). <https://doi.org/10.1007/s13369-021-05648-x>
- W.A. Shaltout, G.A. El-Naggar, G. Esmail, A.F. Hassan, Synthesis and characterization of ferric@nanocellulose/nanohydroxyapatite bio-composite based on sea scallop shells and cotton stalks: adsorption of Safranin-O dye. *Biomass Convers. Biorefinery.* (2022). <https://doi.org/10.1007/s13399-022-02753-1>
- H. Karimi-Maleh, A. Ayati, R. Davoodi, B. Tanhaei, F. Karimi, S. Malekmohammadi, Y. Orooji, L. Fu, M. Sillanpää, Recent advances in using of chitosan-based adsorbents for removal of pharmaceutical contaminants: a review. *J. Clean. Prod.* **291**, 125880 (2021). <https://doi.org/10.1016/j.jclepro.2021.125880>
- R. Boopathy, T. Das, New approach of integrated advanced oxidation processes for the treatment of lube oil processing wastewater. *Arab. J. Sci. Eng.* **43**, 6229–6236 (2018). <https://doi.org/10.1007/s13369-018-3417-6>
- H. Ghasemi, S. Mozaffari, S.H. Mousavi, B. Aghabarari, N. Abu-Zahra, Decolorization of wastewater by heterogeneous Fenton reaction using MnO₂-Fe₃O₄/CuO hybrid catalysts. *J. Environ. Chem. Eng.* **9**, 105091 (2021). <https://doi.org/10.1016/j.jece.2021.105091>
- S. Mansoori, R. Davarnejad, E.J. Ozumchelouei, A.F. Ismail, Activated biochar supported iron-copper oxide bimetallic catalyst for degradation of ciprofloxacin via photo-assisted electro-Fenton process: a mild pH condition. *J. Water Process Eng.* **39**, 101888 (2021). <https://doi.org/10.1016/j.jwpe.2020.101888>
- K. Sharma, P. Raizada, A. Hossseini-Bandegharai, P. Thakur, R. Kumar, V.K. Thakur, V.H. Nguyen, S. Pardeep, Fabrication of efficient CuO/graphitic carbon nitride based heterogeneous

- photo-Fenton like catalyst for degradation of 2, 4 dimethyl phenol. *Process Saf. Environ. Prot.* **142**, 63–75 (2020). <https://doi.org/10.1016/j.psep.2020.06.003>
9. R. Bulánek, R. Hrdina, A.F. Hassan, Preparation of polyvinylpyrrolidone modified nanomagnetite for degradation of nicotine by heterogeneous Fenton process. *J. Environ. Chem. Eng.* **7**, 102988 (2019). <https://doi.org/10.1016/J.JECE.2019.102988>
 10. R.H. Thabet, M.A. Tony, S.A. El Sherbiny, I.A. Ali, M.K. Fouad, Catalytic oxidation over nanostructured heterogeneous process as an effective tool for environmental remediation. *IOP Conf. Ser. Mater. Sci. Eng.* **975**, 012004 (2020). <https://doi.org/10.1088/1757-899X/975/1/012004>
 11. H. Ghasemi, B. Aghabarari, M. Alizadeh, A. Khanlarkhani, N. Abu-Zahra, High efficiency decolorization of wastewater by Fenton catalyst: magnetic iron-copper hybrid oxides. *J. Water Process Eng.* **37**, 101540 (2020). <https://doi.org/10.1016/J.JWPE.2020.101540>
 12. S.B. Hammouda, N. Adhoum, L. Monser, Synthesis of magnetic alginate beads based on Fe₃O₄ nanoparticles for the removal of 3-methylindole from aqueous solution using Fenton process. *J. Hazard. Mater.* **294**, 128–136 (2015). <https://doi.org/10.1016/J.JHAZMAT.2015.03.068>
 13. N. Panda, H. Sahoo, S. Mohapatra, Decolourization of methyl orange using Fenton-like mesoporous Fe₂O₃-SiO₂ composite. *J. Hazard. Mater.* **185**, 359–365 (2011). <https://doi.org/10.1016/J.JHAZMAT.2010.09.042>
 14. R.C.C. Costa, M.F.F. Lelis, L.C.A. Oliveira, J.D. Fabris, J.D. Ardisson, R.R.V.A. Rios, C.N. Silva, R.M. Lago, Novel active heterogeneous Fenton system based on Fe₃-xMxO₄ (Fe Co, Mn, Ni): the role of M²⁺ species on the reactivity towards H₂O₂ reactions. *J. Hazard. Mater.* **129**, 171–178 (2006). <https://doi.org/10.1016/J.JHAZMAT.2005.08.028>
 15. J. Tang, J. Wang, Fe-based metal organic framework/graphene oxide composite as an efficient catalyst for Fenton-like degradation of methyl orange. *RSC Adv.* **7**, 50829–50837 (2017). <https://doi.org/10.1039/c7ra10145g>
 16. Y. Zhou, Y. Zhang, Z. Li, C. Hao, Y. Wang, Y. Li, Y. Dang, X. Sun, G. Han, Y. Fu, Oxygen reduction reaction electrocatalysis inducing Fenton-like processes with enhanced electrocatalytic performance based on mesoporous ZnO/CuO cathodes: Treatment of organic wastewater and catalytic principle. *Chemosphere* **259**, 127463 (2020). <https://doi.org/10.1016/j.chemosphere.2020.127463>
 17. C. Lai, X. Shi, L. Li, M. Cheng, X. Liu, S. Liu, B. Li, H. Yi, L. Qin, M. Zhang, N. An, Enhancing iron redox cycling for promoting heterogeneous Fenton performance: a review. *Sci. Total Environ.* **775**, 145850 (2021). <https://doi.org/10.1016/j.scitotenv.2021.145850>
 18. S. Wu, J. Guo, Y. Wang, C. Huang, Y. Hu, Facile preparation of magnetic sodium alginate/carboxymethyl cellulose composite hydrogel for removal of heavy metal ions from aqueous solution. *J. Mater. Sci.* **56**(23), 13096–13107 (2021). <https://doi.org/10.1007/s10853-021-06044-4>
 19. S. Pavithra, G. Thandapani, S. Sugashini, P.N. Sudha, H.H. Alkhamis, A.F. Alrefaei et al., Batch adsorption studies on surface tailored chitosan/orange peel hydrogel composite for the removal of Cr(VI) and Cu(II) ions from synthetic wastewater. *Chemosphere* **271**, 129415 (2021). <https://doi.org/10.1016/j.chemosphere.2020.129415>
 20. H. Shehzad, E. Ahmed, M.I. Din, Z.H. Farooqi, M. Arshad, A. Sharif et al., Facile synthesis of novel carboxymethyl-chitosan/sodium alginate grafted with amino-carbamate moiety/bentonite clay composite for effective biosorption of Ni (II) from aqueous solution. *J. Phys. Chem.* **235**(5), 583–607 (2021). <https://doi.org/10.1515/zpch-2019-1555>
 21. Y. Peiyu, Y. Fei, Y. Zhengqu, Z. Xiaochen, M. Jie, Graphene oxide modified κ-carrageenan/sodium alginate double-network hydrogel for effective adsorption of antibiotics in a batch and fixed-bed column system. *Sci. Total Environ.* **837**, 155662 (2022). <https://doi.org/10.1016/j.scitotenv.2022.155662>
 22. A. Muthuvei, M. Jothibas, C. Manoharan, Synthesis of copper oxide nanoparticles by chemical and biogenic methods: photocatalytic degradation and in vitro antioxidant activity. *Nanotechnol. Environ. Eng.* **5**, 1–19 (2020). <https://doi.org/10.1007/s41204-020-00078-w>
 23. T.H. Tran, V.T. Nguyen, Copper oxide nanomaterials prepared by solution methods, some properties, and potential applications: a brief review. *Int. Sch. Res. Not.* **2014**, 1–14 (2014). <https://doi.org/10.1155/2014/856592>
 24. E.N. Bakatula, D. Richard, C.M. Neculita, G.J. Zagury, Determination of point of zero charge of natural organic materials. *Environ. Sci. Pollut. Res.* **25**, 7823–7833 (2018). <https://doi.org/10.1007/s11356-017-1115-7>
 25. I. Langmuir, The adsorption of gases on plane surfaces of glass, mica and platinum. *J. Am. Chem. Soc.* **40**, 1361 (1918). <https://doi.org/10.1021/ja02242a004>
 26. H.M.F. Freundlich, Over the adsorption in solution. *J. Phys. Chem.* **57**, 385–471 (1906)
 27. A.F. Hassan, R. Hrdina, Enhanced removal of arsenic from aqueous medium by modified silica nanospheres: kinetic and thermodynamic studies. *Arab. J. Sci. Eng.* (2021). <https://doi.org/10.1007/s13369-021-05357-5>
 28. S.K. Lagergren, About the theory of so-called adsorption of soluble substances. *Sven Vetenskapsakad Handlingar* **24**, 1–39 (1898)
 29. A.F. Hassan, A.A. Mustafa, G. Esmail, A.M. Awad, Adsorption and photo-fenton degradation of methylene blue using nanomagnetite/potassium carrageenan bio-composite beads. *Arab. J. Sci. Eng.* (2022). <https://doi.org/10.1007/s13369-022-07075-y>
 30. S.A. Idrees, S.A. Naman, A. Shorachi, Kinetic and thermodynamic study of Trifluralin photo-degradation by ultra violet light. *IOP Conf. Ser. Mater. Sci. Eng.* **454**, 012045 (2018). <https://doi.org/10.1088/1757-899X/454/1/012045>
 31. M. Zulfikar, S. Sufian, N.E. Rabat, N. Mansor, Development of Photo-Fenton oxidation as green strategy for phenol degradation enhancement via DMF-controlled TiO₂nanotubes under various oxidizing agents. *J. Environ. Chem. Eng.* **9**, 104933 (2021). <https://doi.org/10.1016/j.jece.2020.104933>
 32. N. Topnani, S. Kushwaha, T. Athar, Wet synthesis of copper oxide nanopowder. *Int. J. Green Nanotechnol. Mater. Sci. Eng.* **1**, 37–41 (2010). <https://doi.org/10.1080/19430840903430220>
 33. A.S. Prasad, Green synthesis and spectral analysis of surface encapsulated copper (II) oxide nanostructures. *Mater. Sci. Pol.* **37**, 503–509 (2019). <https://doi.org/10.2478/msp-2019-0062>
 34. H. Wang, Q. Shen, X. Li, F. Liu, Fabrication of copper oxide dumbbell-like architectures via the hydrophobic interaction of adsorbed hydrocarbon chains. *Langmuir* **25**, 3152–3158 (2009). <https://doi.org/10.1021/la803276z>
 35. G. Mohammadnezhad, F. Ariaeinezhad, F. Steiniger, Magnetite/κ-carrageenan nanocomposites: a convenient recyclable tool for Cu(II) ions adsorption from aqueous solution. *Inorg. Chem. Res.* **3**, 129–144 (2019). <https://doi.org/10.22036/icr.2020.209416.1056>
 36. Y. Bagbi, A. Sarswat, D. Mohan, A. Pandey, P.R. Solanki, Lead and chromium adsorption from water using L-cysteine functionalized magnetite (Fe₃O₄) nanoparticles. *Sci. Rep.* **7**, 1–15 (2017). <https://doi.org/10.1038/s41598-017-03380-x>
 37. S.K. Shinde, D.P. Dubal, G.S. Ghodake, V.J. Fulari, Hierarchical 3D-flower-like CuO nanostructure on copper foil for supercapacitors. *RSC Adv.* **5**, 4443–4447 (2015). <https://doi.org/10.1039/c4ra11164h>

38. T. Tenkyong, N. Bachan, J. Raja, P.N. Kumar, J.M. Shyla, Investigation of sol-gel processed CuO/SiO₂ nanocomposite as a potential photoanode material. *Mater. Sci. Pol.* **33**, 826–834 (2015). <https://doi.org/10.1515/msp-2015-0097>
39. D. Zhang, J. Qin, D. Wei, S. Yang, S. Wang, C. Hu, Enhancing the CO preferential oxidation (CO-PROX) of CuO–CeO₂/reduced graphene oxide (rGO) by conductive rGO-wrapping based on the interfacial charge transfer. *Catal. Lett.* **148**, 3454–3466 (2018). <https://doi.org/10.1007/s10562-018-2520-3>
40. A.F. Hassan, H. Elhadidy, Effect of Zr⁺⁴ doping on characteristics and sonocatalytic activity of TiO₂/carbon nanotubes composite catalyst for degradation of chlorpyrifos. *J. Phys. Chem. Solids.* **129**, 180–187 (2019). <https://doi.org/10.1016/j.jpcs.2019.01.018>
41. A.K. Zharmagambetova, E.T. Talgatov, A.S. Auyezkhanova, N.Z. Tumabayev, F.U. Bukharbayeva, Effect of polyvinylpyrrolidone on the catalytic properties of Pd/γ-Fe₂O₃ in phenylacetylene hydrogenation. *React. Kinet. Mech. Catal.* **131**, 153–166 (2020). <https://doi.org/10.1007/s11144-020-01857-x>
42. A. Eslami, N.M. Juibari, S.G. Hosseini, M. Abbasi, Synthesis and characterization of CuO nanoparticles by the chemical liquid deposition method and investigation of its catalytic effect on the thermal decomposition of ammonium perchlorate. *Cent. Eur. J. Energ. Mater.* **14**, 152–168 (2017). <https://doi.org/10.2221/cejem/67560>
43. S. Di Bucchianico, M.R. Fabbri, S.K. Misra, E. Valsami-Jones, D. Berhanu, P. Reip, E. Bergamaschi, L. Migliore, Multiple cytotoxic and genotoxic effects induced in vitro by differently shaped copper oxide nanomaterials. *Mutagenesis* **28**, 287–299 (2013). <https://doi.org/10.1093/mutage/get014>
44. G.A. Kloster, N.E. Marcovich, M.A. Mosiewicki, Composite films based on chitosan and nanomagnetite. *Eur. Polym. J.* **66**, 386–396 (2015). <https://doi.org/10.1016/j.eurpolymj.2015.02.042>
45. A.S. Bhatt, D. Krishna Bhat, M.S. Santosh, Electrical and magnetic properties of chitosan-magnetite nanocomposites. *Phys. B Condens. Matter.* **405**, 2078–2082 (2010). <https://doi.org/10.1016/j.physb.2010.01.106>
46. T.V. Thi, A.K. Rai, J. Gim, J. Kim, Potassium-doped copper oxide nanoparticles synthesized by a solvothermal method as an anode material for high-performance lithium ion secondary battery. *Appl. Surf. Sci.* **305**, 617–625 (2014). <https://doi.org/10.1016/j.apsusc.2014.03.144>
47. M. Khan, A. Khan, H. Khan, N. Ali, S. Sartaj, S. Malik, N. Ali, H. Khan, S. Shah, M. Bilal, Development and characterization of regenerable chitosan-coated nickel selenide nano-photocatalytic system for decontamination of toxic azo dyes. *Int. J. Biol. Macromol.* **182**, 866–878 (2021). <https://doi.org/10.1016/j.ijbiomac.2021.03.192>
48. S.U. Din, A. Azeez, Zain-ul-Abdin, S. Haq, M. Hafeez, M. Imran, S. Hussain, S.S. Alarfaji, Investigation on cadmium ions removal from water by a nanomagnetite based biochar derived from *eleocharis dulcis*. *J. Inorg. Organomet. Polym. Mater.* **31**, 415–425 (2021). <https://doi.org/10.1007/s10904-020-01758-5>
49. N. Benhadria, M. Hachemaoui, F. Zaoui, A. Mokhtar, S. Boukeris, T. Attar, L. Belarbi, B. Boukoussa, Catalytic reduction of methylene blue dye by copper oxide nanoparticles. *J. Clust. Sci.* (2021). <https://doi.org/10.1007/s10876-020-01950-0>
50. A. Santha, R. Varghese, H. Joy Prabu, I. Johnson, D. Magimai Antoni Raj, S. John Sundaram, Production of sustainable biofuel from biogenic waste using CuO nanoparticles as heterogeneous catalyst. *Mater. Today Proc.* **36**, 447–452 (2019). <https://doi.org/10.1016/j.matpr.2020.05.069>
51. G. Song, Y. Shi, A. Li, H. Wang, G. Ding, Facile preparation of three-dimensional graphene oxide/κ-carrageenan composite aerogel and its efficient ability for selective adsorption of methylene blue. *J. Mater. Sci.* **56**, 14866–14879 (2021). <https://doi.org/10.1007/s10853-021-06211-7>
52. M. Ariannezhad, D. Habibi, S. Heydari, V. Khorramabadi, The nano-magnetite-loaded 2-mercaptobenzoxazole as an adsorbent for the selective removal of the Pb²⁺, Ni²⁺ and Cd²⁺ ions from aqueous solutions. *Korean J. Chem. Eng.* **38**, 1510–1521 (2021). <https://doi.org/10.1007/s11814-021-0792-6>
53. A.H. Nordin, K. Ahmad, L.K. Xin, W. Syieluing, N. Ngadi, Efficient adsorptive removal of methylene blue from synthetic dye wastewater by green alginate modified with pandan. *Mater. Today Proc.* **39**, 979–982 (2019). <https://doi.org/10.1016/j.matpr.2020.04.564>
54. S.M. Khoshkho, B. Tanhaei, A. Ayati, M. Kazemi, Preparation and characterization of ionic and non-ionic surfactants impregnated κ-carrageenan hydrogel beads for investigation of the adsorptive mechanism of cationic dye to develop for biomedical applications. *J. Mol. Liq.* **324**, 115118 (2021). <https://doi.org/10.1016/j.molliq.2020.115118>
55. E.A. Moawed, A.B. Abulkibash, Selective separation of Light green and Safranin O from aqueous solution using *Salvadora persica* (Miswak) powder as a new biosorbent. *J. Saudi Chem. Soc.* **20**, S178–S185 (2016). <https://doi.org/10.1016/j.jscs.2012.10.011>
56. A.F. Hassan, Synthesis of carbon nano-onion embedded metal-organic frameworks as an efficient adsorbent for cadmium ions: kinetic and thermodynamic studies. *Environ. Sci. Pollut. Res.* **26**, 24099–24111 (2019). <https://doi.org/10.1007/s11356-019-05581-5>
57. H.T. Dinh, N.T. Tran, D.X. Trinh, Investigation into the adsorption of methylene blue and methyl orange by UiO-66-NO₂ nanoparticles. *J. Anal. Methods Chem.* (2021). <https://doi.org/10.1155/2021/5512174>
58. M. Shaban, M.R. Abukhadra, A.S. Mohamed, M.G. Shahien, S.S. Ibrahim, Synthesis of mesoporous graphite functionalized by nitrogen for efficient removal of safranin dye utilizing rice husk ash; equilibrium studies and response surface optimization. *J. Inorg. Organomet. Polym. Mater.* **28**, 279–294 (2018). <https://doi.org/10.1007/s10904-017-0726-2>
59. S.N. Tambat, P.K. Sane, S. Suresh, O.N. Varadan, A.B. Pandit, S.M. Sontakke, Hydrothermal synthesis of NH₂-UiO-66 and its application for adsorptive removal of dye. *Adv. Powder Technol.* **29**, 2626–2632 (2018). <https://doi.org/10.1016/j.apt.2018.07.010>
60. H.K. Boparai, M. Joseph, D.M. O'Carroll, Kinetics and thermodynamics of cadmium ion removal by adsorption onto nano zerovalent iron particles. *J. Hazard. Mater.* **186**, 458–465 (2011). <https://doi.org/10.1016/j.jhazmat.2010.11.029>
61. K.H. Kamal, S. Dacrory, S.S.M. Ali, K.A. Ali, S. Kamel, Adsorption of Fe ions by modified carrageenan beads with tricarboxy cellulose: kinetics study and four isotherm models. *Desalin. Water Treat.* **165**, 281–289 (2019). <https://doi.org/10.5004/dwt.2019.24560>
62. R. Hamzenejad Taghliabad, E. Sepehr, H. Khodaverdiloo, A. Samadi, M.H. Rasouli-Sadaghiani, Characterization of cadmium adsorption on two cost-effective biochars for water treatment. *Arab. J. Geosci.* (2020). <https://doi.org/10.1007/s12517-020-05477-6>
63. Z. Zhang, L. Xu, Y. Liu, R. Feng, T. Zou, Y. Zhang, Y. Kang, P. Zhou, Efficient removal of methylene blue using the mesoporous activated carbon obtained from mangosteen peel wastes: Kinetic, equilibrium, and thermodynamic studies. *Microporous Mesoporous Mater.* **315**, 110904 (2021). <https://doi.org/10.1016/j.micromeso.2021.110904>
64. Z. Shi, R. Zhang, J. Zhang, Role of weak magnetic field for enhanced oxidation of orange G by magnetic Fenton. *Environ. Sci. Pollut. Res. Int.* (2021). <https://doi.org/10.1007/s11356-021-14887-2>
65. M. Fayazi, Preparation and characterization of carbon nanotubes/pyrite nanocomposite for degradation of methylene blue by a

- heterogeneous Fenton reaction. *J. Taiwan Inst. Chem. Eng.* **120**, 229–235 (2021). <https://doi.org/10.1016/J.JTICE.2021.03.033>
66. N.K. Daud, B.H. Hameed, Decolorization of Acid Red 1 by Fenton-like process using rice husk ash-based catalyst. *J. Hazard. Mater.* **176**, 938–944 (2010). <https://doi.org/10.1016/J.JHAZMAT.2009.11.130>
 67. S.P. Sun, A.T. Lemley, p-Nitrophenol degradation by a heterogeneous Fenton-like reaction on nano-magnetite: process optimization, kinetics, and degradation pathways. *J. Mol. Catal. A Chem.* **349**, 71–79 (2011). <https://doi.org/10.1016/J.MOLCATA.2011.08.022>
 68. S.T. Liu, J. Huang, Y. Ye, A.B. Zhang, L. Pan, X.G. Chen, Microwave enhanced Fenton process for the removal of methylene blue from aqueous solution. *Chem. Eng. J.* **215–216**, 586–590 (2013). <https://doi.org/10.1016/J.CEJ.2012.11.003>
 69. S. Hu, H. Yao, K. Wang, C. Lu, Y. Wu, Intensify removal of nitrobenzene from aqueous solution using nano-zero valent iron/granular activated carbon composite as fenton-like catalyst. *Water Air Soil Pollut.* (2015). <https://doi.org/10.1007/s11270-015-2421-7>
 70. A.F. Hassan, H. Elhadidy, A.M. Abdel-Mohsen, Adsorption and photocatalytic detoxification of diazinon using iron and nanotitania modified activated carbons. *J. Taiwan Inst. Chem. Eng.* **75**, 299–306 (2017). <https://doi.org/10.1016/J.JTICE.2017.03.026>
 71. B. Jain, A.K. Singh, K. Hyunook, E. Lichtfouse, V.K. Sharma, Treatment of organic pollutants by homogeneous and heterogeneous Fenton reaction processes. *Environ. Chem. Lett.* **16**, 947–967 (2018). <https://doi.org/10.1007/s10311-018-0738-3>
 72. I. Raheb, M.S. Manlla, Kinetic and thermodynamic studies of the degradation of methylene blue by photo-Fenton reaction. *Helvion.* **7**, e07427 (2021). <https://doi.org/10.1016/J.HELIVION.2021.E07427>
 73. J. Khan, M. Tariq, M. Muhammad, M.H. Mehmood, I. Ullah, A. Raziq, F. Akbar, M. Saqib, A. Rahim, A. Niaz, Kinetic and thermodynamic study of oxidative degradation of acid yellow 17 dye by Fenton-like process: effect of HCO_3^- , CO_3^{2-} , Cl^- and SO_4^{2-} on dye degradation. *Bull. Chem. Soc. Ethiop.* **33**, 243–254 (2019). <https://doi.org/10.4314/bcse.v33i2.5>
 74. U.J. Ahile, R.A. Wuana, A.U. Itodo, R. Sha'Ato, R.F. Dantas, Stability of iron chelates during photo-Fenton process: the role of pH, hydroxyl radical attack and temperature. *J. Water Process Eng.* **36**, 101320 (2020). <https://doi.org/10.1016/J.JWPE.2020.101320>
 75. G.K.R. Angaru, Y.L. Choi, L.P. Lingamdinne, J.S. Choi, D.S. Kim, J.R. Koduru, J.K. Yang, Y.Y. Chang, Facile synthesis of economical feasible fly ash-based zeolite-supported nano zerovalent iron and nickel bimetallic composite for the potential removal of heavy metals from industrial effluents. *Chemosphere* **267**, 128889 (2021). <https://doi.org/10.1016/J.CHEMOSPHERE.2020.128889>
 76. A. Tabatabaefar, A.R. Keshtkar, M. Talebi, H. Abolghasemi, Polyvinyl Alcohol/Alginate/Zelite nanohybrid for removal of metals. *Chem. Eng. Technol.* **43**, 343–354 (2020). <https://doi.org/10.1002/ceat.201900231>
 77. M. Shafiee, M.A. Abedi, S. Abbasizadeh, R.K. Sheshdeh, S.E. Mousavi, S. Shohani, Effect of zeolite hydroxyl active site distribution on adsorption of Pb(II) and Ni(II) pollutants from water system by polymeric nanofibers. *Sep. Sci. Technol.* **55**, 1994–2011 (2020). <https://doi.org/10.1080/01496395.2019.1624572>
 78. F. Bavarsiha, M. Rajabi, M. Montazeri-Pour, Synthesis of $\text{SrFe}_{12}\text{O}_{19}/\text{SiO}_2/\text{TiO}_2$ composites with core/shell/shell nanostructure and evaluation of their photo-catalytic efficiency for degradation of methylene blue. *J. Mater. Sci. Mater. Electron.* **29**, 1877–1887 (2018). <https://doi.org/10.1007/s10854-017-8098-5>
 79. T. Shi, J. Peng, J. Chen, C. Sun, H. He, Heterogeneous photo-fenton degradation of norfloxacin with Fe_3O_4 -multiwalled carbon nanotubes in aqueous solution. *Catal. Lett.* **147**, 1598–1607 (2026). <https://doi.org/10.1007/s10562-017-2026-4>
 80. X. Zhu, L. Zhang, G. Zou, Q. Chen, Y. Guo, S. Liang, L. Hu, M. North, H. Xie, Carboxylcellulose hydrogel confined- Fe_3O_4 nanoparticles catalyst for Fenton-like degradation of Rhodamine B. *Int. J. Biol. Macromol.* **180**, 792–803 (2021). <https://doi.org/10.1016/j.ijbiomac.2021.04.067>

Publisher's Note Springer Nature remains neutral with regard to jurisdictional claims in published maps and institutional affiliations.

Authors and Affiliations

Asaad. F. Hassan¹  · Laila M. Alshandoudi² · Aya M. Awad¹ · Ahmed A. Mustafa¹ · Ghada Esmail¹

✉ Asaad. F. Hassan
asmz68@sci.dmu.edu.eg

¹ Chemistry Department, Faculty of Science, Damanhour University, Damanhour, Egypt

² Science Department, Al Rustaq College of Education, University of Technology and Applied Sciences, Al Rustaq, Sultanate of Oman